

Summary Report for the CONSET Program at AEDC

W. D. Williams and J. W. L. Lewis
ARO, Inc.

September 1980

Final Report for Period July 1973 – December 1979

Approved for public release; distribution unlimited.

**ARNOLD ENGINEERING DEVELOPMENT CENTER
ARNOLD AIR FORCE STATION, TENNESSEE
AIR FORCE SYSTEMS COMMAND
UNITED STATES AIR FORCE**

NOTICES

When U. S. Government drawings, specifications, or other data are used for any purpose other than a definitely related Government procurement operation, the Government thereby incurs no responsibility nor any obligation whatsoever, and the fact that the Government may have formulated, furnished, or in any way supplied the said drawings, specifications, or other data, is not to be regarded by implication or otherwise, or in any manner licensing the holder or any other person or corporation, or conveying any rights or permission to manufacture, use, or sell any patented invention that may in any way be related thereto.

Qualified users may obtain copies of this report from the Defense Technical Information Center.

References to named commercial products in this report are not to be considered in any sense as an endorsement of the product by the United States Air Force or the Government.

This report has been reviewed by the Office of Public Affairs (PA) and is releasable to the National Technical Information Service (NTIS). At NTIS, it will be available to the general public, including foreign nations.

APPROVAL STATEMENT

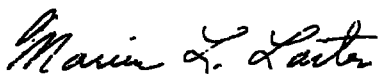
This report has been reviewed and approved.



KENNETH H. LENERS, Captain, USAF
Project Manager
Directorate of Technology

Approved for publication:

FOR THE COMMANDER



MARION L. LASTER
Director of Technology
Deputy for Operations

UNCLASSIFIED

REPORT DOCUMENTATION PAGE		READ INSTRUCTIONS BEFORE COMPLETING FORM
1 REPORT NUMBER AEDC-TR-80-16	2 GOVT ACCESSION NO.	3. RECIPIENT'S CATALOG NUMBER
4 TITLE (and Subtitle) SUMMARY REPORT FOR THE CONSET PROGRAM AT AEDC		5 TYPE OF REPORT & PERIOD COVERED Final Report, July 1973 to December 1979
		6 PERFORMING ORG. REPORT NUMBER
7. AUTHOR(s) W. D. Williams and J. W. L. Lewis, ARO, Inc., a Sverdrup Corporation Company		8 CONTRACT OR GRANT NUMBER(s)
9 PERFORMING ORGANIZATION NAME AND ADDRESS Arnold Engineering Development Center Air Force Systems Command Arnold Air Force Station, TN 37389		10 PROGRAM ELEMENT, PROJECT, TASK AREA & WORK UNIT NUMBERS Program Elements 62302F 921E04
11 CONTROLLING OFFICE NAME AND ADDRESS Arnold Engineering Development Center/DOS Air Force Systems Command Arnold Air Force Station, TN 37389		12. REPORT DATE September 1980
14 MONITORING AGENCY NAME & ADDRESS (if different from Controlling Office)		13 NUMBER OF PAGES 60
		15. SECURITY CLASS. (of this report) UNCLASSIFIED
		15a. DECLASSIFICATION DOWNGRADING SCHEDULE N/A
16 DISTRIBUTION STATEMENT (of this Report) Approved for public release; distribution unlimited.		
17 DISTRIBUTION STATEMENT (of the abstract entered in Block 20, if different from Report)		
18 SUPPLEMENTARY NOTES Available in Defense Technical Information Center (DTIC)		
19 KEY WORDS (Continue on reverse side if necessary and identify by block number) flow-fields expansion gases flow diagnostics laser-Rayleigh/Raman scattering mass spectrometers electron beams fluorescence		
20 ABSTRACT (Continue on reverse side if necessary and identify by block number) From FY74 through FY78, an experimental study of the condensation of gases in expansion flow fields has been conducted under the auspices of the AFRPL CONSET Program. Pure gas expansions, as well as binary and ternary gas mixture expansions and the plume of a monopropellant hydrazine thruster have been studied. Laser-Rayleigh and laser-Raman scattering, mass spectrometric sampling, and electron beam fluorescence were used as nonperturbing flow diagnostics. The results of these experiments are summarized in this technical report.		

UNCLASSIFIED

PREFACE

The work reported herein was conducted by the Arnold Engineering Development Center (AEDC), Air Force Systems Command (AFSC), at the request of the Air Force Rocket Propulsion Laboratory, AFSC. The results of the research were obtained by ARO, Inc., AEDC Division (a Sverdrup Corporation Company), operating contractor for the AEDC, AFSC, Arnold Air Force Station, Tennessee, under ARO Project Numbers V34S-R9A, V34S-B3A, V32S-11A, V32S-51A, and VF449. The final project manager for AFRPL was Lt. Eric Lund, and Captain Stanislaus L. Ludwig was the final Air Force project manager for AEDC. The data analysis was completed on May 25, 1979, and the manuscript was submitted for publication on March 13, 1980.

CONTENTS

	<u>Page</u>
1.0 INTRODUCTION	
1.1 Program Background	7
1.2 Objectives	8
1.3 Rayleigh Scattering Technique	9
1.4 Raman Scattering and Electron Beam Fluorescence	10
1.5 Mass Spectrometric Sampling	11
2.0 DESCRIPTION OF EXPERIMENTAL SETUP FOR SCALING LAW AND SIMULATED THRUSTER STUDIES	
2.1 Research Vacuum Chamber	11
2.2 Gas Flow Sources	11
2.3 Optical System	12
3.0 DESCRIPTION OF EXPERIMENTAL SETUP FOR MONOPROPELLANT THRUSTER STUDIES	
3.1 Research Vacuum Chamber	13
3.2 Thruster	13
3.3 Diagnostic Systems	13
4.0 DISCUSSION OF SCALING LAW DATA	
4.1 Rayleigh Scattering Results from the Scaling Law Experiments	14
4.2 Description of Scaling Analysis	16
4.3 Correlation of Static Property Measurements, Rayleigh Scattering Measurements, and Theoretical Predictions with Condensation	17
5.0 DISCUSSION OF THRUSTER AND SIMULATED THRUSTER DATA	
5.1 Thruster Results	18
5.2 Simulated Thruster Results	20
6.0 SUMMARY	
6.1 Conclusions	21
6.2 Recommendations for Future Work	23
REFERENCES	24

ILLUSTRATIONS

<u>Figure</u>	<u>Page</u>
1. Experimental Arrangement for the Scaling Law and Simulated Thruster Studies	27
2. Sonic Orifice and Conical Nozzle Schematics	27
3. Thruster Installation in the RVC	28
4. Experimental Arrangement for Special Diagnostic Instrumentation for Thruster Studies	28
5. Axial Variation of $I'(II)$ for All N_2 Reservoir Pressures and Sonic Orifice Diameters Investigated	29
6. Axial Variation of $I'(II)$ for All O_2 Reservoir Pressures Investigated, Sonic Orifice	29
7. Axial Variation of $I'(II)$ for All CO Reservoir Pressures Investigated, Sonic Orifice	30
8. Axial Variation of $I'(II)$ for All Ar Reservoir Pressures Investigated, Sonic Orifice	30
9. Axial Variation of $I'(II)$ for All N_2 Reservoir Pressures Investigated, $\theta_{1/2} = 5.63$ deg	31
10. Axial Variation of $I'(II)$ for all N_2 Reservoir Pressures Investigated, $\theta_{1/2} = 9.0$ deg	31
11. Axial Variation of $I'(II)$ for all N_2 Reservoir Pressures Investigated, $\theta_{1/2} = 14.5$ deg	32
12. Axial Variation of $I'(II)$ for all O_2 Reservoir Pressures Investigated, $\theta_{1/2} = 10.5$ deg	32
13. Axial Variation of $I'(II)$ for all CO Reservoir Pressures Investigated, $\theta_{1/2} = 10.5$ deg	33
14. Axial Variation of $I'(II)$ for all NO Reservoir Pressures Investigated, $\theta_{1/2} = 10.5$ deg	33
15. Axial Variation of $I'(II)$ for all HCl Reservoir Pressures Investigated, $\theta_{1/2} = 10.5$ deg	34
16. Axial Variation of $I'(II)$ for all H_2O Reservoir Pressures Investigated, $\theta_{1/2} = 10.5$ deg	35
17. Axial Variation of $I'(II)$ for all CO_2 Reservoir Pressures Investigated, $\theta_{1/2} = 10.5$ deg	36
18. Axial Variation of $I'(II)$ for all Ar Reservoir Pressures Investigated, $\theta_{1/2} = 10.5$ deg	36
19. Axial Variation of $I'(II)$ for all N_2 Reservoir Temperatures Investigated, $\theta_{1/2} = 10.5$ deg	37

<u>Figure</u>	<u>Page</u>
20. Axial Variation of $I'(\parallel)$ for all O_2 Reservoir Temperatures Investigated, $\theta_{1/2} = 10.5$ deg	37
21. Axial Variation of $I'(\parallel)$ for all CO Reservoir Temperatures Investigated, $\theta_{1/2} = 10.5$ deg	38
22. Axial Variation of $I'(\parallel)$ for all HCl Reservoir Temperatures Investigated, $\theta_{1/2} = 10.5$ deg	38
23. Axial Variation of $I'(\parallel)$ for all CO_2 Reservoir Temperatures Investigated, $\theta_{1/2} = 10.5$ deg	39
24. Axial Variation of $I'(\parallel)$ for all Ar Reservoir Temperatures Investigated, $\theta_{1/2} = 10.5$ deg	39
25. Radial Variation of $I'(\parallel)$ for an N_2 Reservoir Pressure of 10.2 atm at Three Axial Positions, $\theta_{1/2} = 14.5$ deg	40
26. Radial Variation of $I'(\parallel)$ for an N_2 Reservoir Pressure of 7.85 atm at Six Axial Positions, $T_o = 288$ K, $\theta_{1/2} = 10.5$ deg	41
27. Radial Variation of $I'(\parallel)$ for an N_2 Reservoir Pressure of 7.85 atm at Six Axial Positions, $T_o = 355$ K, $\theta_{1/2} = 10.5$ deg	41
28. Axial Variation of $I'(\parallel)$ for a 95-percent N_2 /5-percent CO_2 Mixture, $\theta_{1/2} = 9.0$ deg	42
29. Axial Variation of $I'(\parallel)$ for a 90-percent N_2 /10-percent CO_2 Mixture, $\theta_{1/2} = 10.5$ deg	42
30. Axial Variation of Scattering Function, f , for 14.5-deg Nozzle, N_2 Gas, P_o Variation	43
31. Axial Variation of Scattering Function, f , for Sonic Orifice, $D = 1.325$ mm, N_2 Gas	43
32. Axial Variation of Scattering Function, f , for 10.5-deg Nozzle, N_2 Gas, T_o Variation	44
33. Diagram of Expansion Process	44
34. N_2 and O_2 Condensation Onset Locus Using Reduced Values	45
35. Ar and CO Condensation Onset Locus Using Reduced Values	45
36. HCl and NO Condensation Onset Locus Using Reduced Values	46
37. CO_2 and H_2O Condensation Onset Locus Using Reduced Values	46
38. Axial Variation of $I'(\parallel)$, Number Density, Temperature, Mass Fraction (g), and Depolarization Ratio: 14.5-deg Conical Nozzle, $P_o = 10.2$ atm, N_2	47
39. Axial Variation of $I'(\parallel)$, Number Density, Temperature, and Mass Fraction: 14.5-deg Conical Nozzle, $P_o = 6.80$ atm, N_2	47
40. Laser Scattering Measurements in the New and Simulated Thruster Plumes	48

<u>Figure</u>	<u>Page</u>
41. Axial Variation of the Scattering Function, f , in the New Thruster Plume	48
42. Variation of Rayleigh Scattering in the New Thruster Plume with Reservoir Parameters at Axial Position $\hat{x} = 45.2$	49

TABLES

1. Saturation and Condensation Onset Parameters	50
2. Sonic Orifice Scaling Constants	54
3. Conical Nozzle Scaling Constants	54
4. Lennard-Jones 12-6 Intermolecular Potential Constants	55
5. Comparison of Rayleigh Scattering Data for the Aged, New, and Simulated Thruster Plumes	56
6. Rayleigh Scattering Intensity, New Thruster Plume, Test Period No. 25, $\hat{x} = 45.2$	57
7. Rayleigh Scattering Intensity, New Thruster Plume, Test Period No. 26	58
NOMENCLATURE	59

1.0 INTRODUCTION

1.1 PROGRAM BACKGROUND

Extensive work has been devoted to the development of infrared detection systems for a variety of orbital surveillance functions. Various thrusters are used aboard satellites for attitude control and station-keeping purposes, and interest in condensation phenomena within the plumes of these thrusters was stimulated by the realization that gaseous plume constituents could condense into conglomerates of larger particles which could ultimately pass within the field of view of the infrared detection system. These conglomerates could affect the satellite-borne sensors by several mechanisms:

1. The conglomerates can a) emit or b) absorb electromagnetic radiation within the spectral region to which the infrared detection system is sensitive.
2. The conglomerates can provide large electromagnetic radiation scattering centers which can scatter radiation to the detector from a source normally out of the field of view.

As a result, the sensor's background noise can be increased, false target information can be provided, and the sensitivity of the detector can be decreased.

In FY73 initial experimental studies of plume condensation were begun under the Air Force Rocket Propulsion Laboratory (AFRPL) CONSCAT Program. The objectives of this program were to determine the amount of Rayleigh scattered radiation from the homogeneous nucleation of nitrogen (N_2) in a supersonic flow from a conical nozzle for a known incident radiant energy at a particular visible wavelength. Infrared scattering was to be inferred by using the Rayleigh scattering relations (Refs. 1 through 3).

The axial profiles of Rayleigh scattered intensity were in good agreement with the intensity levels expected for an isentropic, uncondensed N_2 expansion for low reservoir pressure and the dimensionless axial position $\hat{x} = x/D$, where D is a characteristic throat diameter for the gas source. The scattered intensity showed a subsequent sharp increase with \hat{x} at low-to-intermediate reservoir pressures, which was interpreted as indicating that condensation onset was occurring. With continued increasing \hat{x} , the scattering signal went through a maximum and then decayed. This behavior was interpreted as indicating condensate growth followed by cessation of the condensation process. An analytic method was developed to calculate condensation and cluster growth. Knowledge of the experimental

scattering results enabled selection of initial nucleation conditions for the calculation such that the calculated properties of condensed N₂ nozzle flow such as gas density, temperature, spatial locations of onset and cessation of condensation, and Rayleigh scattered intensity were in satisfactory agreement with the experimental results. Condensate mass fractions of 10⁻² or less produced experimentally observable increases in the rotational temperature of the gas. However, no noticeable change in the monomer number density was detected. Estimates of condensate cluster diameter ($\approx 100 \text{ \AA}$) supported the validity of the application of Rayleigh scattering for the study of the condensation process in expansion flows.

1.2 OBJECTIVES

It was concluded in Ref. 1 that in order to develop an a priori condensation calculation procedure for a wide range of flow conditions one must have knowledge of the scaling laws of condensation for flow source geometry, reservoir conditions, and molecular parameters. Consequently, the CONSET Program was formulated with the objective of determining experimentally the onset and growth properties of condensate clusters in typical exhaust plume flow fields and the dependence of the condensation process on nozzle geometry, reservoir conditions, molecular parameters, and flow composition. The program was initially divided into three task areas. The first task was to investigate the effects of variation of reservoir pressure and temperature, throat diameter, and nozzle expansion angle on the spatial laws of condensation onset and growth for N₂ flowfields. The second task was to extend the condensation scaling law study to other species such as argon (Ar), oxygen (O₂), carbon monoxide (CO), nitric oxide (NO), carbon dioxide (CO₂), ammonia (NH₃), water vapor (H₂O), and hydrogen chloride (HCl), as well as some binary mixtures of these species. The third task was to investigate the condensation process in both an actual thruster plume and a simulated thruster plume. The actual thruster to be used was a 0.1-lbf monopropellant hydrazine engine.

The experimental investigations were conducted using four noninterfering, nonperturbing flow diagnostic techniques. Laser-Rayleigh scattering was used to characterize the distribution and growth of clusters as well as condensation onset. Laser-Raman scattering was used for measurement of plume species number density and temperature in the higher density, near-field region of the expansion, and electron beam fluorescence was used for measurement of N₂ gas density and temperature in the far field of the expansion. The mass spectrometer probe was used for far-field measurements of the monopropellant thruster relative species concentrations.

1.3 RAYLEIGH SCATTERING TECHNIQUE

The basic equations and rationale for the application of Rayleigh scattering to the study of condensing gas flow fields have been given in detail in Refs. 4 and 5. Therefore, only a brief summary need be given in this report.

For an incident laser beam of wavelength λ_0 and intensity I_0 focused within a flowing pure gas sample of number density n with species polarizability α , the scattered intensity, I , which is normalized by I_0 , is given by

$$I = Kn\alpha^2/\lambda_0^4 \quad (1)$$

in which K is a coefficient containing transmission and calibration factors. For a scatterer of radius "a" which is characterized by bulk properties, it is known that α is proportional to a^3 , which indicates the sensitivity of Rayleigh scattering to scatterer size. Assuming the condensing flow field to be composed of a collection of gas phase monomers and molecular clusters, or i -mers, where i is the number of molecules per cluster, the single Rayleigh scattering intensity with polarization vector parallel to the incident beam's plane of polarization is

$$I'(\parallel) = \sum_{i=1}^{\infty} \left(\frac{n_i}{n_0} \right) \left(\frac{\alpha_i}{\alpha_1} \right)^2 \quad (2)$$

where n_0 is the reservoir number density of the flow field. The scattered intensity $I'(\parallel)$ includes the further normalization provided by the scattered intensity from a collection of monomers of number density n_0 .

For an uncondensed, isentropic expansion,

$$I'(\parallel) = \left(\frac{n_1}{n_0} \right)^0 = I^0(\parallel) \quad (3)$$

Super- and subscript zeros denote isentropic and reservoir conditions, respectively. The axial variation of $I^0(\parallel)$ is provided by the method-of-characteristics solution (MOCS) (Ref. 6) for nozzle flow and by the Sherman-Ashkenas theory (Ref. 7) for sonic orifice flow.

Deviation of the measured $I'(ll)$ from $I''(ll)$ indicates, for these studies, the existence of condensation. A direct measure of the existence of clusters within the flow is given by the scattering function, f , which is written as

$$f = \left(\frac{I'(ll)}{I''(ll)} \right) - 1 \quad (4)$$

Although the scattering function, f , is an ambiguous measure of the simultaneous increase in the mean cluster size and condensate mole fraction, the axial variation of f as a function of reservoir conditions and nozzle geometry yields empirical condensation scaling laws.

1.4 RAMAN SCATTERING AND ELECTRON BEAM FLUORESCENCE

Laser-Raman scattering and electron beam fluorescence were the diagnostic techniques used for plume static property measurements in the near and far fields, respectively. The use of the electron beam-induced fluorescence radiation resulting from inelastic electron-molecule collisions for the measurement of N_2 gas density and temperature in flow fields has been discussed and demonstrated in detail in Refs. 5 and 8. Briefly, a high-energy beam of electrons produces excited electronic states upon impact with N_2 molecular species. By radiative decay these states produce a fluorescence, and, assuming no collisional quenching effects, the intensity of the fluorescence is directly proportional to the N_2 gas density. The electron beam technique is normally used at total gas number densities of less than 10^{15} cm^{-3} (Ref. 9) to avoid collisional quenching effects, and for that reason the technique is generally a far-field plume diagnostic. The molecular fluorescence consists of vibrational-rotational band structure within the electronic transition systems, which, upon spectral dispersion, yields the temperature of the rotational energy mode (Ref. 8).

As a result of nonresonant, inelastic collisions between laser beam photons and gas molecules, radiation is scattered from the beam at frequencies other than that of the laser light. This phenomenon, spontaneous Raman scattering, is discussed in detail in Refs. 10 through 13, and details of application to measurement of species number density and temperature are fully discussed in Ref. 14. Briefly, a high-energy laser beam interacts with gas molecules and causes changes in the rotational and vibrational energy levels. As a result, the Raman scattered radiation consists of molecularly specific pure rotational lines as well as vibrational-rotational band structure from which rotational and vibrational temperatures can be determined. The intensity of the lines and bands is also directly proportional to the molecular species number density. Because it is a scattering process, the Raman intensity is not subject to collisional quenching effects; therefore, the Raman technique is useful in the near-field plume. However, the low Raman scattering cross section ($\approx 10^{-28} \text{ cm}^2/\text{sr}$) generally prevents use of the technique for far-field measurements.

1.5 MASS SPECTROMETRIC SAMPLING

The direct-sampling mass spectrometer probe developed at AEDC (Ref. 15) was used for species mole fraction measurements on the axial centerline of the monopropellant hydrazine thruster. In reality, the probe is merely a miniature molecular beam system which uses a quadrupole mass spectrometer as the detector. Immersing the probe in the exhaust plume of a rocket engine forms a molecular beam of exhaust products which is directed into the sampling volume of the mass spectrometer ion source. Subsequently, ions are created, extracted, and directed through a mass discriminator and then into an electron multiplier. The result is a set of measurable signals that are proportional to the number densities of molecules in the exhaust plume which (after ionization) possess particular charge-to-mass ratios. The interpretation of the signals is dependent upon a reliable calibration, a knowledge of the additional daughter mass peaks (cracking patterns) created in the ion source from plume parent constituents, and the ability to maintain the very stringent vacuum conditions necessary to operate a molecular beam system.

2.0 DESCRIPTION OF EXPERIMENTAL SETUP FOR SCALING LAW AND SIMULATED THRUSTER STUDIES

2.1 RESEARCH VACUUM CHAMBER

The experiments reported herein were conducted using the 4- by 10-ft Research Vacuum Chamber (RVC), a stainless steel vacuum chamber nominally 4 ft (1.3 m) in diameter and 10 ft (3.3 m) long. The chamber, shown in Fig. 1, is constructed in two sections: a movable section approximately 4 ft (1.3 m) long and a stationary section approximately 6 ft (2 m) long. An additional spool piece 1.5 ft (0.49 m) long was used to provide eight instrumentation ports.

Initial pumping capabilities were supplied by a 300-cfm mechanical pump for rough pumping and a 6-in.-diam oil diffusion pump with a baffle refrigerated by liquid nitrogen for intermediate pumping. Pumping during experiments was provided by a finned, gaseous helium cyroliner at 20 K with a liquid nitrogen cyroliner radiation shield located in the stationary section of the RVC. The blank-off chamber pressure achieved was approximately 10^{-7} torr.

2.2 GAS FLOW SOURCES

The flow generators were sonic orifices and conical nozzles attached to a GTE-Sylvania heated source. This assembly was mounted on a motor-driven, three-dimensional traversing mechanism located in the movable section of the RVC. The sonic orifices were 1.325, 3.2,

and 3.05 mm in diameter with a diameter-to-thickness ratio greater than 20. The conical nozzles had a nominal throat diameter and nozzle length of 1.0 and 5.334 mm, respectively. The four nozzle half-angles were 14.5, 10.5, 9.0, and 5.63 deg. Schematics of the sonic orifice and conical nozzle are shown in Fig. 2. The conical nozzle for the simulated thruster studies was fabricated to duplicate the nozzle of the monopropellant thruster. The half-angle was 15 deg, and the throat diameter was 0.03 in. (0.76 mm). The length from the throat to the exit plane was 0.356 in. (9.04 mm), and the expansion ratio was 55.3.

The gas reservoir was instrumented with standard, calibrated pressure and temperature gages. Gases were supplied from high-pressure bottles, and two 25.0-nanometer (nm) filters were installed in the inlet line to minimize effects of particulate matter.

2.3 OPTICAL SYSTEM

An argon-ion laser operating at a wavelength of 514.5 nm provided excitation for the Rayleigh/Raman scattering measurements. As shown in Fig. 1, the incident laser beam polarization was rotated along the x-direction, expanded, and focused onto the chamber centerline. Light scattered from the focal volume was collected by an f/2 lens system, collimated, and focused onto the input slit of a 0.85-m, double-grating spectrometer. For the Rayleigh scattering measurements, HN-22 Polaroid™ material was placed in the collimated light path, and a polarization scrambler was placed immediately in front of the spectrometer entrance slit. During scaling law studies the entrance slit aperture setting, collection optics magnification, and laser beam focusing together resulted in observation of a 1.5-mm-long, 50- to 100- μ m-diam cylindrical scattering volume. For the simulated thruster measurements a 2.75-mm long, 600- μ m-diam cylindrical scattering volume was observed using an f/4 collection lens system.

The radiation detector was a thermoelectrically cooled photomultiplier, and the output was processed by an Ortec® photon-counting system for either digital display or strip chart recording.

For the electron beam measurements, the laser dump and laser input aperture assembly shown in Fig. 1 were removed and replaced by an RCA Model VC2126V4 electron gun assembly and cylindrical Faraday cup assembly, respectively. The beam was injected into the chamber and flow field through a 1.0-mm-diam orifice which provided the necessary pressure drop to maintain the electron gun pressure at less than 6×10^{-6} torr under nominal chamber vacuum conditions. For number density and temperature measurements the beam current was 1.0 mA at 30keV energy. The collection optics/spectrometer/data acquisition system was the same as that used for the laser scattering measurements.

3.0 DESCRIPTION OF EXPERIMENTAL SETUP FOR MONOPROPELLANT THRUSTER STUDIES

3.1 RESEARCH VACUUM CHAMBER

Figure 3 is a schematic of the monopropellant thruster installation in the RVC. For the thruster experiments the RVC was reconfigured by using the 4-ft-long movable section to house a 37-liter capacity, liquid helium-filled cryopump. The section was placed directly in line with the fixed section housing the cryoliner. Another movable section, approximately 3 ft (0.99 m) long, was connected to the spoolpiece, and it was in this section that the thruster was mounted on the same traversing table as was used for the scaling law experiments.

3.2 THRUSTER

The thruster used in the experimental program was a Hamilton Standard REA/CTS 10-18 monopropellant hydrazine thruster which employed a 30-35 mesh Shell 405 ABSG spontaneous catalyst with a preloaded, packed bed design. The exhaust was provided by a conical nozzle with a 0.76-mm-diam throat and an exit area ratio of 55. The thruster was operated over a thrust range from 0.44 to 1.10 N (0.1 to 0.25 lbf) with a nominal 0.14-second/9.86-sec-off duty cycle using initial catalyst bed temperatures of 367 K (200°F), 478 K (400°F), and 589 K (600°F). The engine was always operated without its heat shield. A complete description of the engine, its properties, propellant system, and method of operation may be found in Ref. 16.

3.3 DIAGNOSTIC SYSTEMS

Exhaust plume diagnostic systems employed included a mass spectrometer probe, a quartz crystal microbalance (QCM), a laser Raman/Rayleigh scattering system, an electron beam fluorescence system, and a particle collection network. The QCM and particle collection network were for providing information on the contamination properties of the exhaust plume rather than for condensation diagnostics; therefore, they are not discussed in this report.

Figure 4 is a schematic diagram of the special diagnostic instrumentation. Laser scattering excitation was provided by a conventional mode ruby laser with a pulse width of approximately 1 msec. The electron beam system was the same as that used for the scaling law studies. A 0.5-m double grating spectrometer was used for spectral dispersion for both laser scattering and electron beam measurements. The quadrupole mass spectrometer/skimmer system was located on the centerline at the axial position $450 \leq x$

≤ 650 . The probe face was conical with a cone half-angle of 30 deg, and a 15-deg conical half-angle, pure nickel skimmer with a 0.020-in.-diam orifice was soldered to the probe body. The forward section of the probe was cooled with gaseous helium at ≈ 20 K.

Mass spectrometer data were displayed on an oscilloscope as well as acquired digitally. Electron beam and laser scattering data were acquired using a cooled photomultiplier tube and photon counting. Data processing and initial analysis of all data were performed using an online PDP-8 computer system with line printer output.

4.0 DISCUSSION OF SCALING LAW DATA

4.1 RAYLEIGH SCATTERING RESULTS FROM THE SCALING LAW EXPERIMENTS

Figures 5 through 8 show the axial profiles of $I'(\parallel)$ for the N_2 , O_2 , CO, and Ar expansions from sonic orifices. Figures 9 through 24 show the axial profiles of $I'(\parallel)$ for the N_2 , O_2 , CO, NO, HCl, H_2O , CO_2 , and Ar expansions from conical nozzles. Theoretical predictions as obtained from the Sherman-Ashkenas theory or the MOCS are also shown. It is observed that the onset of condensation is manifested by a dramatic increase of $I'(\parallel)$ relative to the isentropic prediction. The onset of condensation moves nearer the saturation point as P_o increases or T_o decreases, and, with the exception of the region of discontinuity in the MOCS nozzle calculations, $I'(\parallel)$ is in good agreement with the calculated values prior to condensation onset. Furthermore, with the exception of H_2O and NO, it can be seen that for the lowest P_o values or highest T_o values the metastable gas sample supports a supersaturated state for approximately 30 nozzle throat or sonic orifice diameters before condensing. It is also noted (generally) that the massive condensate growth for the nozzle flows is rather abrupt, whereas the massive condensate growth region for the sonic orifice flow is preceded by a gradual deviation from the isentropic prediction. The magnitude of the Rayleigh scattering intensity in the condensate growth regions is seen to increase rapidly with increasing P_o and to decrease extremely rapidly with increasing T_o .

Radial profiles of $I'(\parallel)$ for N_2 are shown in Figs. 25 through 27. In Figs. 25 and 26 the $\hat{x} = 17.35$ and 17.9 positions, respectively, are interesting in that two scattering peaks are symmetrically located off the axial centerline. Similar observations have been reported by Beylich (Ref. 17) in a study of CO_2 condensation in a nozzle flow. From Figs. 11 and 19, it is seen that condensation on the axial centerline has not begun at $\hat{x} = 17.35$ and 17.9, respectively. However, Figs. 25 and 26 show that onset has already begun for $r/D_t > 0$. Photographic observations of the $\theta_{1/2} = 14.5$ -deg nozzle flow field are presented in Ref. 18, and the nozzle, a dark, isentropic expansion zone, and a bright, hemispherical onset zone

are clearly evident, as is filamentary structure within the condensation growth region. These photographs substantiate the radial profile results of Figs. 25 and 26. The radial profiles of Fig. 27 are interesting because they demonstrate the sensitivity of the condensation process to reservoir temperature. An increase of 67 K in T_o has completely suppressed the off-axis condensation at $\hat{x} = 17.9$. At $\hat{x} = 55.4$, off-axis peaks can again be observed, however.

Figures 28 and 29 are axial variations of $I'(\parallel)$ for 95-percent $N_2/5\text{-percent CO}_2$ and 90-percent $N_2/10\text{-percent CO}_2$ mixtures, respectively. As demonstrated in Ref. 19, a simple computation of reservoir partial pressures and reference to the pure gas axial variations of $I'(\parallel)$ for the appropriate nozzle reveal that $I'(\parallel)$ has been greatly enhanced relative to the level expected based on the pure gas expansions. Saturation locations, \hat{x}_s , are indicated in Figs. 28 and 29 for both CO_2 and N_2 . Obviously CO_2 is the initiator of the onset, because N_2 is not supersaturated in the region of onset. These results demonstrate the important role of mixed clusters in gas mixture condensation processes.

Figures 30 through 32 demonstrate the axial variation of the scattering function, f , for N_2 gas for conical nozzles (Figs. 30 and 32) and a sonic orifice (Fig. 31). These plots are rather typical of all the f -versus- x plots obtained in the scaling law study for those gases which exhibit condensation onset external to the nozzle. It is noted that in these semilogarithmic plots the f values for a given P_o (or T_o) and nozzle (or orifice) form straight lines, and it is the intersection of these straight lines with the x -axis that is used to determine the onset of condensate growth. These axial onset locations are denoted by x_θ . The rapid increase in f following onset is obvious, as are the orders of magnitude increase in f as the reservoir pressure increases or reservoir temperature decreases.

The vapor pressure data compiled in either Ref. 20 (Hilsenrath et al.) or Ref. 21 and the isentropic solution for each particular flow field investigated are used to obtain the saturation values of pressure and temperature, P_s and T_s , respectively, as well as similar values at condensation onset, denoted by P_θ and T_θ . The isentropic supersaturation pressure ratio, $(s_\theta)^\circ$, is defined as

$$(s_\theta)^\circ = P_s/P_\theta \quad (5)$$

and the isentropic degrees of supercooling, $(s'_\theta)^\circ$, are defined as

$$(s'_\theta)^\circ = T_s - T_\theta \quad (6)$$

It should be noted that the supersaturation ratio defined here is not the normal definition of the ratio of the pressure at onset to the equilibrium vapor pressure at onset, $P_\theta/P_{v\theta}$. The definition of Eq. (5) is used because of the unreliability of $P_{v\theta}$ values at the low temperatures at condensation onset in the expansion flows of these experiments. The $(s_\theta)^\circ$ values are orders of magnitude lower than the normally defined supersaturation ratios for the flow fields investigated here. These supersaturation parameters are illustrated in Fig. 33, which is a diagram of the expansion process.

Table 1 is a tabulation of the saturation, condensation onset, and supersaturation parameters for the various gases and sources. It is readily observed that \hat{x}_θ approaches \hat{x} , as P_o increases or T_o decreases, and supercooling is seen to range approximately from 30 to 200 K.

4.2 DESCRIPTION OF SCALING ANALYSIS

Empirical functional relations of f with \hat{x} , \hat{x}_θ , P_o , T_o , and D or D_t were obtained (Refs. 22 and 23) using the results of the axial variation of the scattering function data. These variations in the condensate growth region were represented by

$$\hat{x} = \hat{x}_\theta e^{bf} \quad (7)$$

and by graphical determination it was found that

$$b \propto P_o^{-m_0} T_o^{m_1} \quad (8)$$

$$\hat{x}_\theta \propto (P^{m_2} D_{eq})^{-m_3} T_o^{m_4} \quad (9)$$

The quantity D_{eq} is D and $(D_t \cot \theta_{1/2})C(\gamma)$ for sonic orifices and conical nozzles, respectively. The expression $C(\gamma)$ is a parameter dependent upon specific heat ratio and is defined in Ref. 24. The sonic orifice scaling constants are tabulated in Table 2, and the conical nozzle constants are given in Table 3.

By using the well-depth and range parameters, ϵ and σ , respectively, of the Lennard-Jones 12-6 intermolecular potential function, reduced onset pressures (P_θ^*) and temperatures (T_θ^*) have been determined using

$$P_\theta^* = P_\theta / (\epsilon \sigma^3) \quad (10)$$

$$T_\theta^* = T_\theta / (\epsilon / k) \quad (11)$$

where k is Boltzmann's constant. The reduced onset parameters are also given in Table 1, and the intermolecular potential constants which were used are given in Table 4. The loci of condensation onset are shown in Figs. 34 through 37. The common locus for the homonuclear diatomic molecules N_2 and O_2 is observed. In addition, the difference between the Ar results and the results for N_2 and O_2 is noted to illustrate the effect of specific heat ratio upon the location of the onset locus. Not unexpectedly, the loci of polar diatomics such as CO and HCl are found to be substantially different, and this illustrates the inadequacy of the two-parameter Lennard-Jones potential for describing the interaction of polar molecules. As is well known, the interaction of polar molecules includes important contributions from dipole-dipole forces, and the three-parameter Stockmayer potential is more accurate for this description.

4.3 CORRELATION OF STATIC PROPERTY MEASUREMENTS, RAYLEIGH SCATTERING MEASUREMENTS, AND THEORETICAL PREDICTIONS WITH CONDENSATION

Figures 38 and 39 show the measured axial variation of $I'(l)$, $n(N_2)/n_o$, and T/T_o for two P_o values for N_2 nozzle flows. Number density and temperature were obtained using laser-Raman scattering and also by electron beam fluorescence. A more complete exposition of the static parameter measurements of N_2 and other gas species' flows can be found in Refs. 5, 14, 18, and 19, but the measurements shown in Figs. 38 and 39 well illustrate the results of the measurements. As shown in Figs. 38 and 39, the monomer number density is little affected by the condensation process; however, the static temperature can be increased by as much as 50 per cent above the isentropic prediction due to the heat release in the condensation process. It is also observed that the increase in temperature correlates very well with the onset of condensate growth. Not shown in either Fig. 38 or 39 are the far-field measurements of $n(N_2)/n_o$ made with the electron beam system; however, these results are given in Ref. 4 and show excellent agreement with the MOCS prediction.

Predictions of Rayleigh scattering intensity, condensate mass fraction, and static temperature generated using the liquid drop, monodisperse condensation model are also shown in Figs. 38 and 39, as well as in Fig. 19. This model is described in detail in Ref. 18. Briefly, this calculation assumes the condensing flow field to be inviscid, adiabatic, and one-dimensional, with no mass transfer across the stream tube boundary. The gas and condensate are assumed to obey the perfect gas relation. The condensed phase is assumed to be of the form of monodisperse spherical drops or particles which are characterized by bulk properties and to be in the free molecular flow regime relative to the uncondensed phase.

Condensate-gas velocity slip effects are ignored, and the condensate growth rate is determined by gas-condensate interaction only. The mass accommodation coefficient is assumed to be unity. Initial size and number density of spontaneous nucleation sites are adjustable parameters and may be selected so as to reproduce as closely as possible the experimental Rayleigh scattering results. For the predictions shown in Figs. 38, 39, and 19 the initial nucleation sites were chosen to be dimers with mole fractions on the order of 10^{-3} , and the starting point for the calculation was the saturation point, \hat{x}_s . The model can make adequate (± 50 percent) predictions for pure gas expansions of the Rayleigh scattering intensity variation and the location of the condensation onset if the initial nucleation sites are assumed to be dimers with a concentration equal to the equilibrium dimer mole fraction at saturation. The predictions of the model are observed to agree more closely with the experimental measurements as degree of condensation increases. As can be best observed in Fig. 38, the model-predicted temperature increase that results from the condensation process agrees well with the experimentally determined temperatures. Condensate mass fractions on the order of 10^{-2} to 10^{-1} are predicted for the cases shown in Figs. 38, 39, and 19. As noted in Figs. 38 and 39 the number of molecules per cluster is 100, and the size of the clusters is on the order of 10 Å.

Also shown in Figs. 25 and 38 are measurements of the Rayleigh scattering depolarization ratio, ρ , which is defined as

$$\rho = I'(\perp) / I'(\parallel) \quad (12)$$

The axial value of ρ (Fig. 38) does indeed decrease rapidly from its room temperature monomer value as the cluster growth region is entered. Furthermore, the radial value of ρ (Fig. 25) decreases rapidly as the off-axis cluster growth region is entered. This behavior is intuitively expected, because as the linear N₂ molecules cluster together they should form more spherical scatterers that contribute a larger portion to the scattered intensity than do the monomers.

5.0 DISCUSSION OF THRUSTER AND SIMULATED THRUSTER DATA

5.1 THRUSTER RESULTS

The large quantity of data accumulated during the thruster experiments is presented in detail in Refs. 16 and 25; therefore, only data pertinent to the phenomenon of condensation will be discussed here. Rayleigh scattering levels, $I'(\parallel)$, measured in the aged and new thruster plumes are compared in Table 5 for two test conditions (2A and 2S; see Ref. 16). The scattering function, f , was evaluated for a $\gamma = 1.2$ plume expansion and is tabulated in

Table 5. As observed in Table 5, the f factors for the aged thruster are approximately a factor of 50 greater than those for the new thruster. It is believed that the high Rayleigh scattering levels for the aged thruster are a result of raw hydrazine traveling down the axial centerline. This belief is supported by the high mass deposition rate measured on the axial centerline by a QCM, particle sampling measurements, and radial Rayleigh scattering profiles which reveal the extremely high levels only on the axial centerline (see Ref. 16).

The Rayleigh scattering levels for the new thruster are an order of magnitude or more greater than expected for a noncondensing, particulate-free plume expansion as can be observed in Tables 5, 6, and 7 and in Fig. 40, which demonstrates the axial variation of $I'(ll)$ for the new thruster. It can be seen in Fig. 40 that the measured values of $I'(ll)$ exceed the predicted values by a magnitude which increases with increasing \hat{x} , and this is well illustrated by the axial variation of the scattering function, f , plotted in Fig. 41 for thruster test conditions 2S and 2C. Both of these conditions possess an axial coordinate dependence which exhibits a rapid increase at the lower \hat{x} values and becomes asymptotic at $f \approx 100$ for the far-field plume. Although the $I'(ll)$ values for the thruster were obtained using calibration factors appropriate for pure N_2 , the analysis in Ref. 25 has shown that f should be zero with an uncertainty on the order of ± 0.1 for a noncondensing plume expansion of N_2 , H_2 , and NH_3 with $1.2 \leq \gamma \leq 1.3$. The possible presence of either particulate matter or raw fuel droplets cannot explain the Rayleigh scattering results, for if such flow-borne particulates followed the expansion, then f would be approximately constant; if the material were concentrated along the axial streamtube, then f would increase continually with x .

The Raman measurements of temperature and total density in the plume are also shown in Fig. 40; assuming the expansion to have frozen γ and chemistry and using the isentropic relation between temperature and total number density, a plume γ of 1.22 is determined (Ref. 25). The Raman and mass spectrometric measurements of species mole fractions enable the inferential determination of a plume γ of approximately 1.30 (Ref. 25). These results demonstrate that the $\gamma = 1.3$ expansion curve should be followed but that $\gamma = 1.22$ is the actual heat capacity ratio. This situation is indicative of significant condensation in the flow field, and Fig. 13 of Ref. 18 shows a similar expansion history and behavior regarding N_2 condensation. Therefore, the Raman and mass spectrometric measurements as well as the measured magnitude and variation of the Rayleigh scattering function support the contention that significant condensation is occurring in the thruster plume.

Using the results tabulated in Tables 6 and 7, one can scale $I'(ll)$ as a function of reservoir pressure and temperature for an initial catalyst bed temperature of 478 K and for $\hat{x} = 45.2$. The scaling is

$$I'(ll) \propto P_o^{2.5} T_o^{-5}$$

with a correlation coefficient of -0.994. Unfortunately, a change in initial catalyst bed temperature with the average reservoir parameters remaining the same destroys the scaling as shown in Fig. 42. Therefore, it is not possible to use only the reservoir parameters P_o and T_o for scaling of $I'(\parallel)$ in the thruster plume.

5.2 SIMULATED THRUSTER RESULTS

In an additional effort to investigate the large levels of Rayleigh scattering in the thruster plume, the thruster plume expansion was simulated in the RVC. A nozzle assembly was used that duplicated the nozzle of the thruster, and a set of three gas mixtures was prepared by the AEDC Chemical Laboratory to simulate the thruster plume composition. The first two mixtures were prepared to simulate a plume γ of 1.2, and the third mixture simulated a plume γ of 1.25. The first mixture was a binary mixture of N_2 and NH_3 . The NH_3 mole fraction was equal to that predicted by CONTAM II for the thruster test condition 2S, and the N_2 mole fraction was equal to the sum of the H_2 and N_2 mole fractions predicted by CONTAM II for the 2S condition. For the second mixture, the N_2 , H_2 , and NH_3 mole fractions were those predicted by CONTAM II for test condition 2S. The mole fractions of N_2 , H_2 , and NH_3 for the third mixture were determined using Fig. 90 of Ref. 16.

The mixtures were permitted to flow steadily through a heated source/nozzle assembly, and the reservoir pressure and temperature were set to equal the values of the 2S condition as given in Ref. 25. The flow could be maintained for approximately 60 sec when H_2 was a mixture constituent before the RVC pressure reached a level of 10 mtorr.

The results of these experiments are shown in Fig. 40 and are listed in Table 5 for $\hat{x} = 78.5$. It can be observed that the $\gamma = 1.2$ and 1.25 mixtures of N_2 - H_2 - NH_3 have Rayleigh scattering levels that bracket those observed for the new thruster. The f factor for the $\gamma = 1.2$, N_2 - H_2 - NH_3 mixture is approximately a factor of 2 higher and the f factor for the $\gamma = 1.25$, N_2 - H_2 - NH_3 mixture is approximately a factor of 2 lower than the f factor for the new thruster at the 2S condition. An axial variation of Rayleigh scattering for the $\gamma = 1.2$, N_2 - H_2 - NH_3 mixture is also shown in Fig. 40, and it can be observed that the behavior is very similar to that observed for condensation in the pure gas and binary mixture expansions in the scaling law experiments. As \hat{x} decreases, the Rayleigh scattering is observed to approach the level expected for an isentropic, noncondensing expansion. It is speculated that the same behavior would have been observed for the thruster if reliable measurements could have been made for $\hat{x} < 20$.

Analysis of the intersection of N_2H_4 , H_2O , NH_3 , and N_2 vapor pressure curves with $\gamma = 1.2$ and 1.3 isentropes for test condition 2S reservoir conditions (Ref. 25) shows that NH_3

saturation will occur from $\hat{x} = 9.5$ to 34 and that H_2O and N_2H_4 will saturate much earlier. The previous experiments with N_2/CO_2 mixtures indicate that the H_2O and N_2H_4 condensate will provide nucleation sites that will bring about NH_3 condensation near the saturation point. This would explain the lack of a pronounced peak in the Rayleigh scattering axial profiles for the thruster and the presence of the peak for the simulated mixture profile. It is therefore believed that the high levels of Rayleigh scattering in the new thruster plume are a direct result of condensation of gas mixture species in the flow field.

6.0 SUMMARY

6.1 CONCLUSIONS

A multi-year experimental program for characterization of the onset and growth of condensation in expansion flow fields with regard to nozzle geometry, reservoir conditions, molecular parameters, and flow composition has been completed. This report has reviewed the experimental results; a number of conclusions can be made and are listed as follows:

1. The scaling law for the pure gas scattering function can be written as

$$f \propto P_o^{m_0} T_o^{-m_1} D_t^{m_2} / \cot \theta_{1/2} \quad (\text{Conical Nozzles})$$

$$f \propto P_o^{m_0} D^{m_2} \quad (\text{Sonic Orifice})$$

2. The scaling law for axial centerline location of condensation onset for pure gases can be written as

$$\hat{x}_\theta \propto (P_o^{m_2} D_{eq})^{-m_3} T_o^{m_4}$$

3. Intermolecular parameters were used for normalization of the pure gas condensation onset pressure and temperature values, and the condensation onset loci were plotted in the $P^* \text{-} T^*$ plane. These loci represent the practical limit to which a pure gas can be expanded (supercooled) before massive homogeneous condensation begins. The loci are as follows:

$$P_\theta^* = 7.12 \times 10^{-3} T_\theta^{*4.24}$$

Sonic Orifice

$$P_\theta^* = 2.10 \times 10^{-3} T_\theta^{*3.66}$$

Conical Nozzle

Argon

$P_\theta^* = 3.68 \times 10^{-2} T_\theta^{*5.94}$	Sonic Orifice	Nitrogen (N_2), Oxygen (O_2)
$P_\theta^* = 1.02 \times 10^{-2} T_\theta^{*5.16}$	Conical Nozzle	
$P_\theta^* = 1.49 \times 10^{-2} T_\theta^{*5.68}$	Conical Nozzle	Carbon Monoxide (CO)
$P_\theta^* = 8.63 \times 10^{-3} T_\theta^{*5.95}$	Conical Nozzle	
$P_\theta^* = 51.2 T_\theta^{*10.2}$	Conical Nozzle	Hydrogen Chloride (HCl)
$P_\theta^* = 0.191 T_\theta^{*10.1}$	Conical Nozzle	
		Water Vapor (H_2O)

4. The condensation onset loci results imply that classes of molecules well described by the 12-6 Lennard-Jones potential will have common onset loci depending upon the specific heat ratio. However, polar molecules better represented by the 12-6-3 Stockmayer potential do not show common onset loci for common specific heat ratios.
5. A liquid-drop, monodisperse distribution condensation calculation for flow fields of pure gases was developed. This model can make ± 50 -percent predictions of the axial variation of observed Rayleigh scattering by choosing the initial nucleation sites to be dimers and by choosing the initial dimer concentration to be the equilibrium dimer concentration at the saturation point. Furthermore, the model predicts the observed static temperature rise caused by condensation within ± 20 percent. Cluster size and condensate mass fraction are also predicted by the model.
6. Rayleigh scattering radial profiles of pure gas flows have shown that off-axis condensation has significantly preceded the axial phenomenon.

7. Rayleigh scattering axial profiles of binary gas mixtures (N_2/CO_2 and NH_3/N_2) indicate that the nucleation of the easily condensable species (CO_2 and NH_3) will provide nucleation sites that will cause N_2 condensation near the saturation point rather than permitting the large degrees of supercooling observed for the pure gas expansion.
8. Rayleigh scattering measurements as well as Raman scattering and mass spectrometric measurements indicate a significant quantity of condensate in the new (refurbished) thruster plume, and this was subsequently verified by Rayleigh scattering measurements in a particulate-free simulated thruster plume.
9. The Rayleigh scattering intensity from the new thruster plume scales as $P_o^{-2.5}T_o^5$ for a given initial catalyst bed temperature in dramatic contrast to the scaling observed for pure gases. Because of a significant dependence upon initial catalyst temperature, Rayleigh scattering intensity cannot be scaled using only reservoir parameters P_o and T_o .
10. Monopropellant thruster plumes can be successfully simulated using gas mixtures for the purpose of studying condensation phenomena in the plume.

6.2 RECOMMENDATIONS FOR FUTURE WORK

The primary objective for future work concerning flow-field condensation should be to develop an accurate computer code for predicting the effects of condensation in expansion flows. It is recommended that the development of the code proceed in the following fashion.

- a. The present liquid-drop, monodisperse condensate growth model developed at AEDC for predictions of pure gas axial centerline condensation effects should be expanded for the purpose of prediction of off-axis condensation. The results should be compared to the experimental results of this report.
- b. The classical capillarity theory for calculation of the number density of initial nucleation sites and their size should be added to the condensate growth model developed at AEDC. The results should be compared to the experimental results of this report to quantitatively assess the shortcomings of the classical condensation theory.

c. An alternate approach for calculation of the number density and size of initial nucleation sites should be developed, and it should be strictly kinetic in nature. That is, the kinetic formation of dimers, trimers, etc. must be calculated and subsequently used with the condensate growth model. Again, the results should be compared to the experimental results of this report to assess the validity of the model.

REFERENCES

1. Van de Hulst, H. C. *Light Scattering by Small Particles*. John Wiley and Sons, New York, 1957.
2. Born, M. and Wolf, E. *Principles of Optics*. Pergamon Press, Oxford, England, 1965 (Third Edition).
3. Kerker, M. *The Scattering of Light and Other Electromagnetic Radiation*. Academic Press, New York, 1969.
4. Lewis, J. W. L. and Williams, W. D. "Argon Condensation in Free-Jet Expansions." AEDC-TR-74-32 (AD782445), July 1974.
5. Lewis, J. W. L., Williams, W. D., Price, L. L., and Powell, H. M. "Nitrogen Condensation in a Sonic Orifice Expansion Flow." AEDC-TR-74-36 (AD783254), July 1974.
6. Prozan, R. J. Lockheed Report No. HREC A782535, April 1966. Available upon request from the Defence Documentation Center, Cameron Station, VA.
7. Ashkenas, H. and Sherman, F. S. *Rarefied Gas Dynamics*, Fourth Symposium, Vol. II, edited by J. H. de Leeuw. Academic Press, New York, 1966, pp. 84-105.
8. Williams, W. D., Hornkohl, J. O., and Lewis, J. W. L. "Electron Beam Probe for a Low Density Hypersonic Wind Tunnel." AEDC-TR-71-61 (AD727004), July 1971.
9. Price, L. L. and Lewis, J. W. L. "Collisional Quenching of Atomic and Molecular Nitrogen, Part I: Experimental Results." AEDC-TR-75-151 (AD-A018780), December 1975.
10. Placzek, G. "Rayleigh and Raman Scattering." Translated from a publication of the Akademische Verlagsgesellschaft G. m. b. H., Leipzig, 1934, *Handbuch der Radiologie*, Heft 6, Teil 2, pp. 209-374.

11. Placzek, G. and Teller, E. "Die Rotationsstruktur der Ramanbanden Mehratomiger Moleküle" ("Rotation Structure of the Raman Bands of Polyatomic Molecules"). *Zeitschrift fur Physik*, Vol. 31, March 1933.
12. Sushchinskii, M. M. *Raman Spectra of Molecules and Crystals*. Israel Program for Scientific Translations, New York, 1972.
13. Anderson, A., ed. *The Raman Effect, Vol. 2: Applications*. Marcel Dekker, Inc., New York, 1973.
14. Williams, W. D. and Lewis, J. W. L. "Rotational Temperature and Number Density Measurements of N₂, O₂, CO, and CO₂ in a Hypersonic Flow Field Using Laser-Raman Spectroscopy." AEDC-TR-75-37 (AD-A012877), July 1975.
15. McCay, T. D. and Powell, H. M. "Direct Mass Spectrometric Measurements in a Highly Expanded Rocket Exhaust Plume." *Journal of Spacecraft and Rockets*, Vol. 15, No. 3, May-June 1978, pp. 133-138.
16. Williams, W. D., McCay, T. D., Powell, H.M., Weaver, D.P., et al. "Experimental Study of the Plume Characteristics of an Aged Monopropellant Hydrazine Thruster." AEDC-TR-79-2 (AD-A068326), April 1979.
17. Beylich, A. E. "Condensation in Carbon Dioxide Jet Plumes." *AIAA Journal*, Vol. 8, No. 5, May 1970, pp. 965-967.
18. Lewis, J. W. L. and Williams, W. D. "Profile of an Anisentropic Nitrogen Nozzle Expansion." *The Physics of Fluids*, Vol. 19, No. 7, July 1976, pp. 951-959.
19. Lewis, J. W. L., Williams, W. D., and Powell, H. M. "Laser Diagnostics of a Condensing Binary Mixture Expansion Flow Field." *Rarefied Gas Dynamics: Proceedings of the Ninth International Symposium 1974, Vol II*, edited by M. Becker and M. Fiebig. DFVLR Press, Porz Wahn, West Germany, 1974, pp. F7.1-F7.8.
20. Hilsenrath, J. et al. *Tables of Thermal Properties of Gases*. NBS Circular 564, November 1955.
21. Hodgman, C. D., ed. *Handbook of Chemistry and Physics*, 41 Edition, 1959-1960, Chemical Rubber Publishing Co., Cleveland, Ohio.
22. Williams, W. D. and Lewis, J. W. L. "Condensation Scaling Laws for Reservoir and Nozzle Parameters and Gas Species as Determined by Laser Scattering Experiments." AEDC-TR-76-67 (AD-A029733), September 1976.

23. Williams, W. D. and Lewis, J. W. L. "Experimental Study of the Reservoir Temperature Scaling of Condensation in a Conical Nozzle Flowfield." *Rarefied Gas Dynamics: Progress in Astronautics and Aeronautics*, Vol. 51, Part II, edited by J. Leith Potter. American Institute of Aeronautics and Astronautics, New York, 1977.
24. Hagen, O. F. and Obert, W. "Cluster Formation in Expanding Supersonic Jets: Effect of Pressure, Temperature, Nozzle Size, and Test Gas." *The Journal of Chemical Physics*, Vol. 56, 1 March 1972, pp. 1793-1802.
25. Williams, W. D., McCay, T. D., Powell, H. M., and Lewis, J. W. L. "Experimental Study of the Plume Characteristics of a New Monopropellant Hydrazine Thruster." AEDC-TR-79-54 (AD-A080556), January 1980.

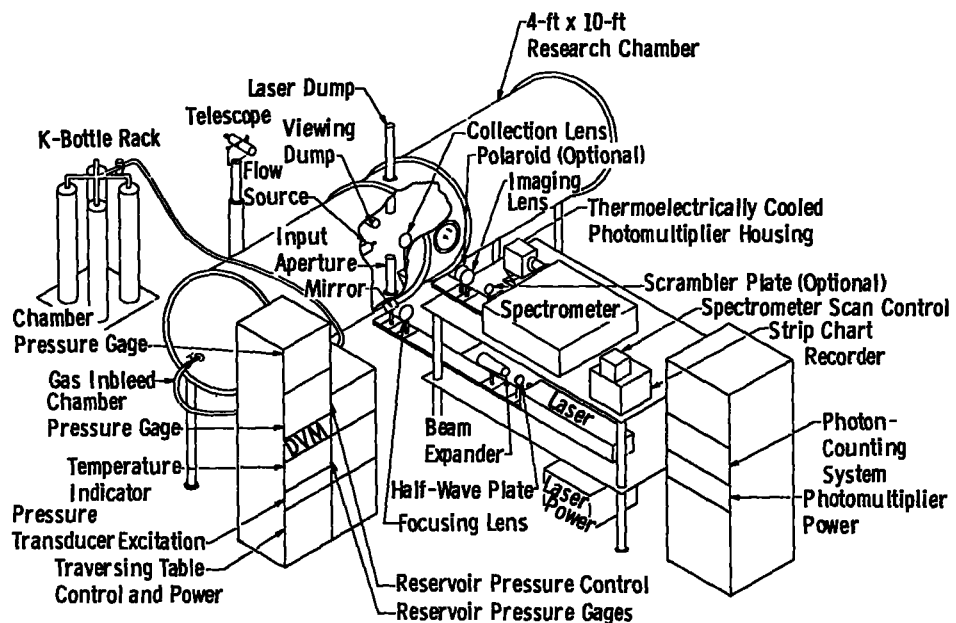


Figure 1. Experimental arrangement for the scaling law and simulated thruster studies.

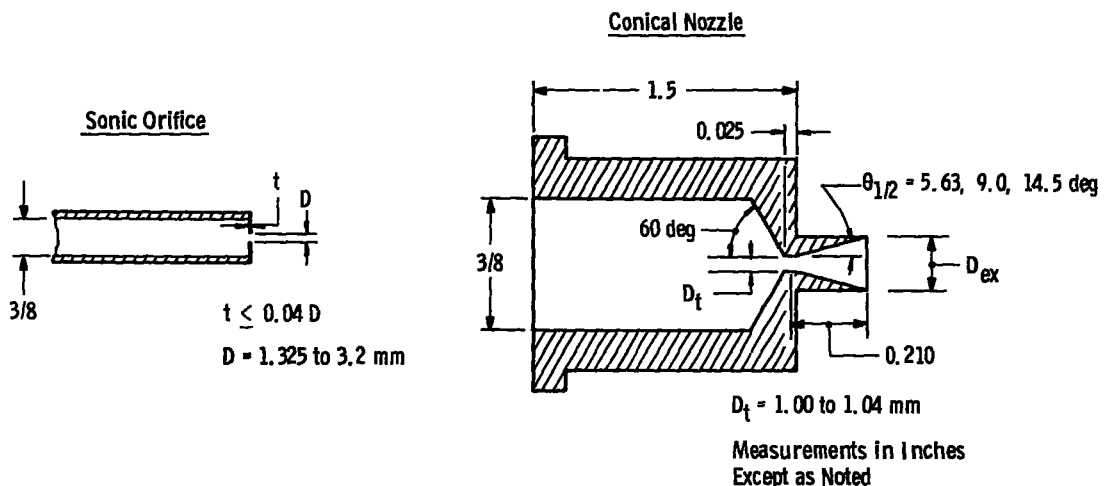


Figure 2. Sonic orifice and conical nozzle schematics.

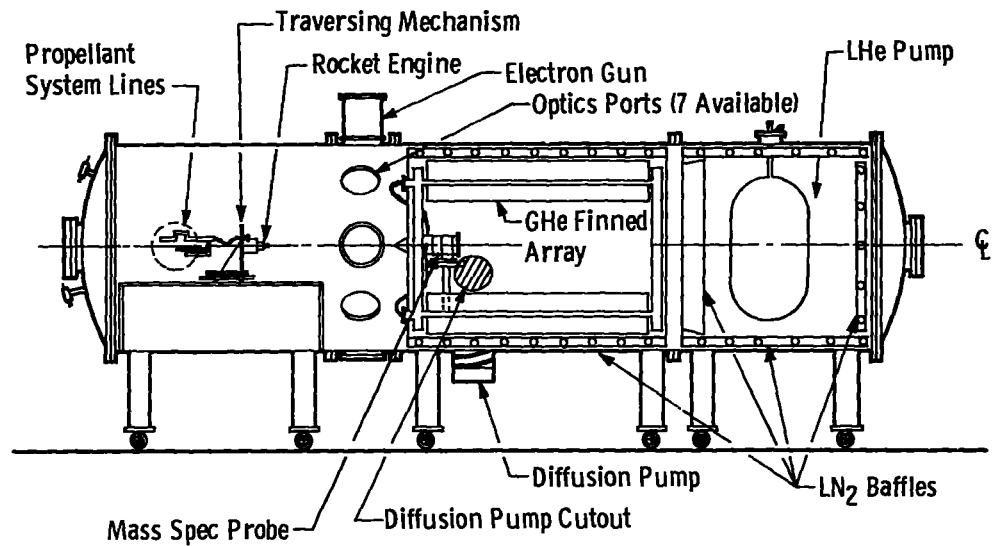


Figure 3. Thruster installation in the RVC.

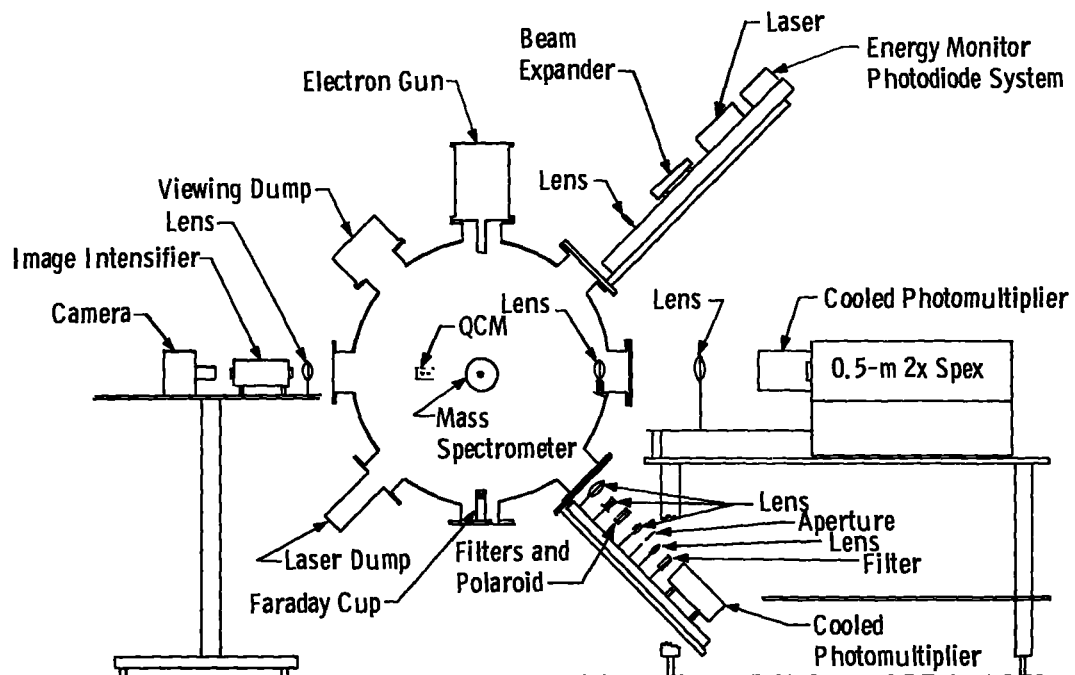


Figure 4. Experimental arrangement for special diagnostic instrumentation for thruster studies.

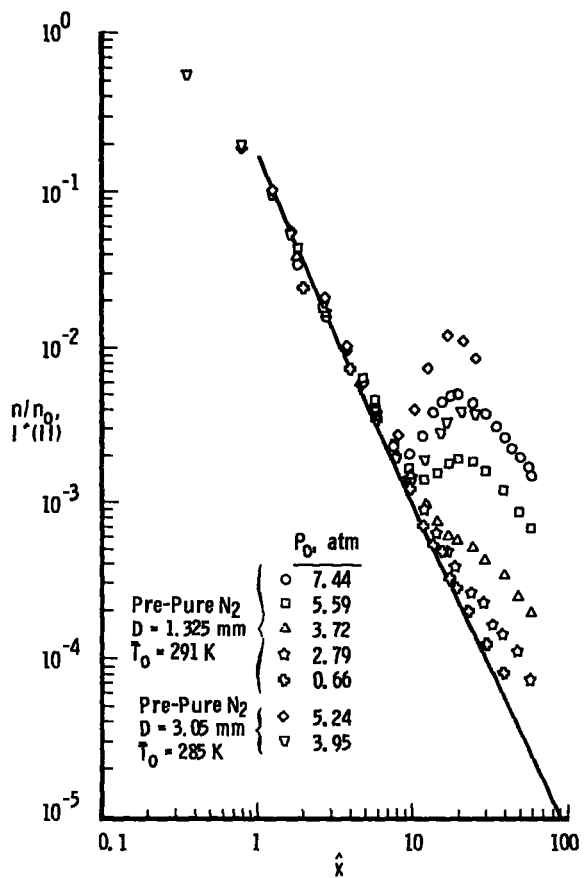


Figure 5. Axial variation of $I' (||)$ for all N_2 reservoir pressures and sonic orifice diameters investigated.

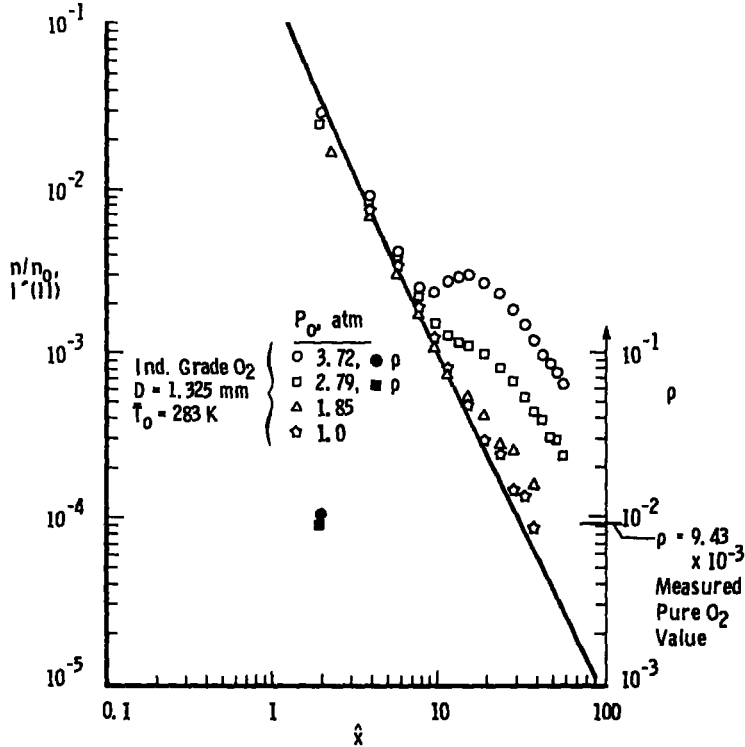


Figure 6. Axial variation of $I' (||)$ for all O_2 reservoir pressures investigated, sonic orifice.

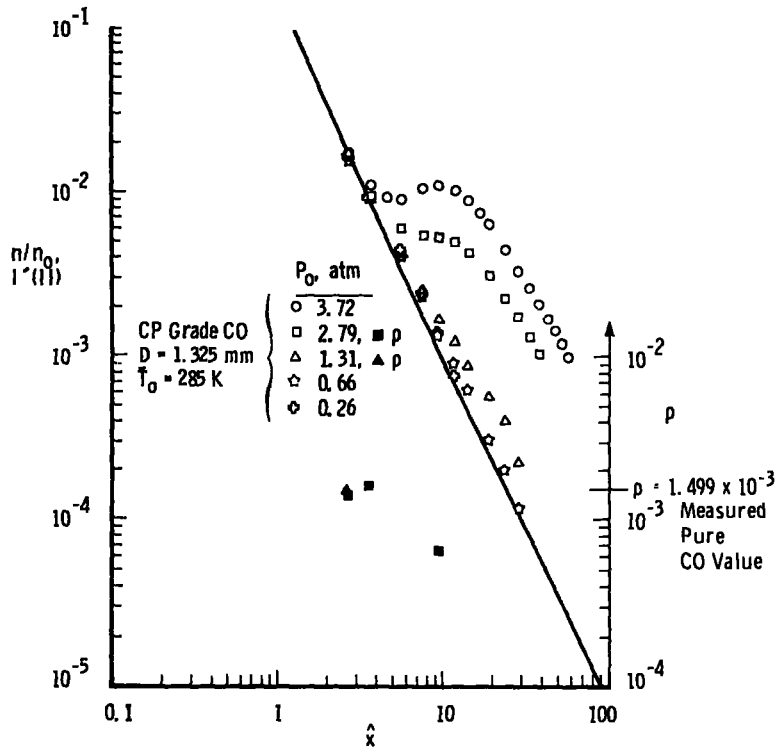


Figure 7. Axial variation of $I'(\parallel)$ for all CO reservoir pressures investigated, sonic orifice.

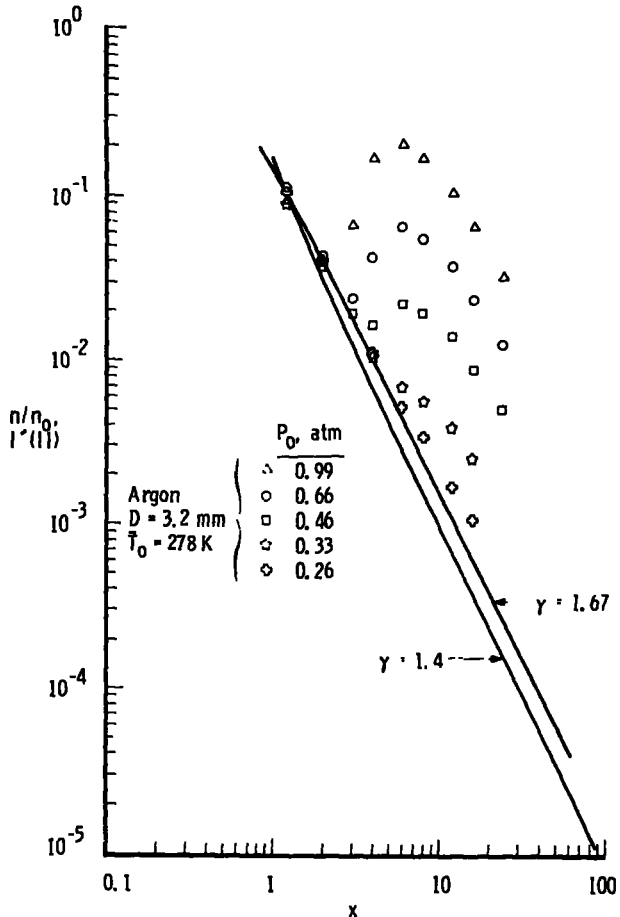


Figure 8. Axial variation of $I'(\parallel)$ for all Ar reservoir pressures investigated, sonic orifice.

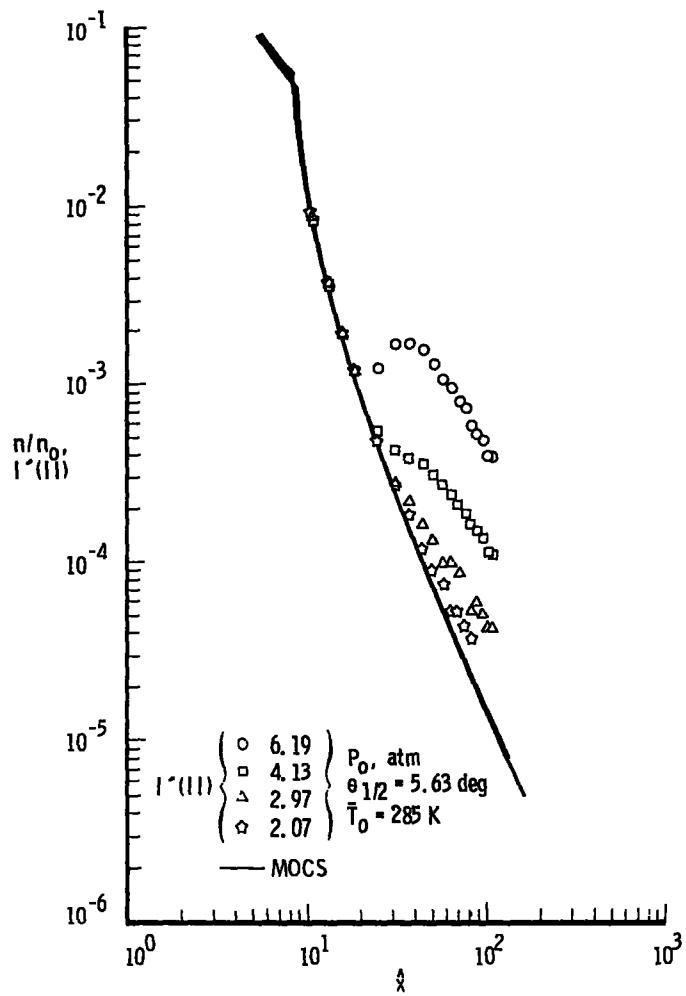


Figure 9. Axial variation of $I'(||)$ for all N_2 reservoir pressures investigated, $\theta_{1/2} = 5.63$ deg.

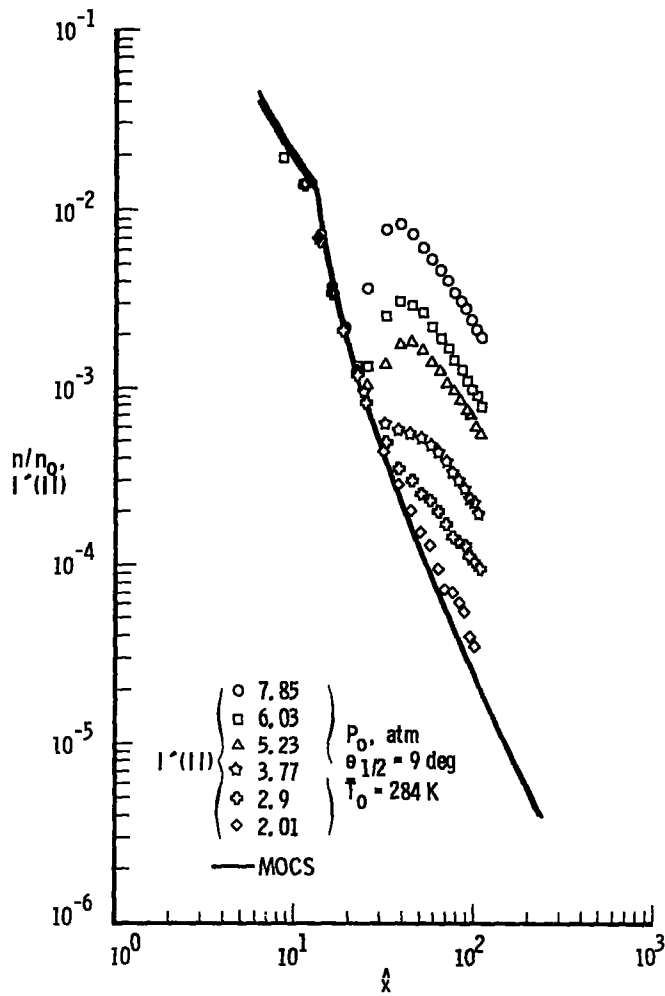


Figure 10. Axial variation of $I'(||)$ for all N_2 reservoir pressures investigated, $\theta_{1/2} = 9.0$ deg.

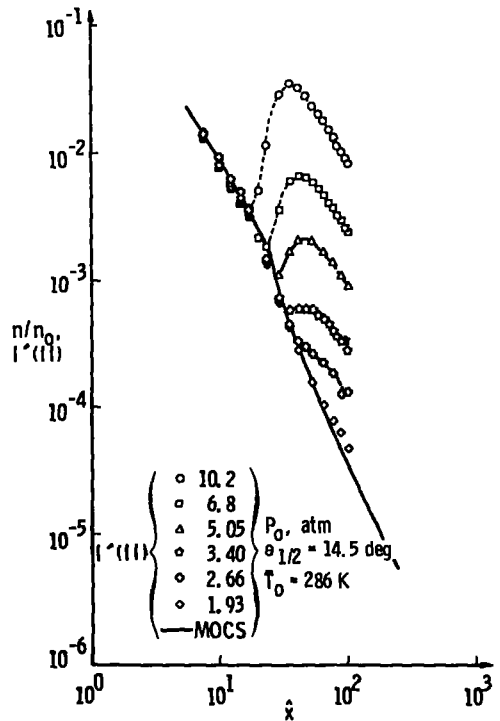


Figure 11. Axial variation of $I'(||)$ for all N_2 reservoir pressures investigated,
 $\theta_{1/2} = 14.5$ deg.

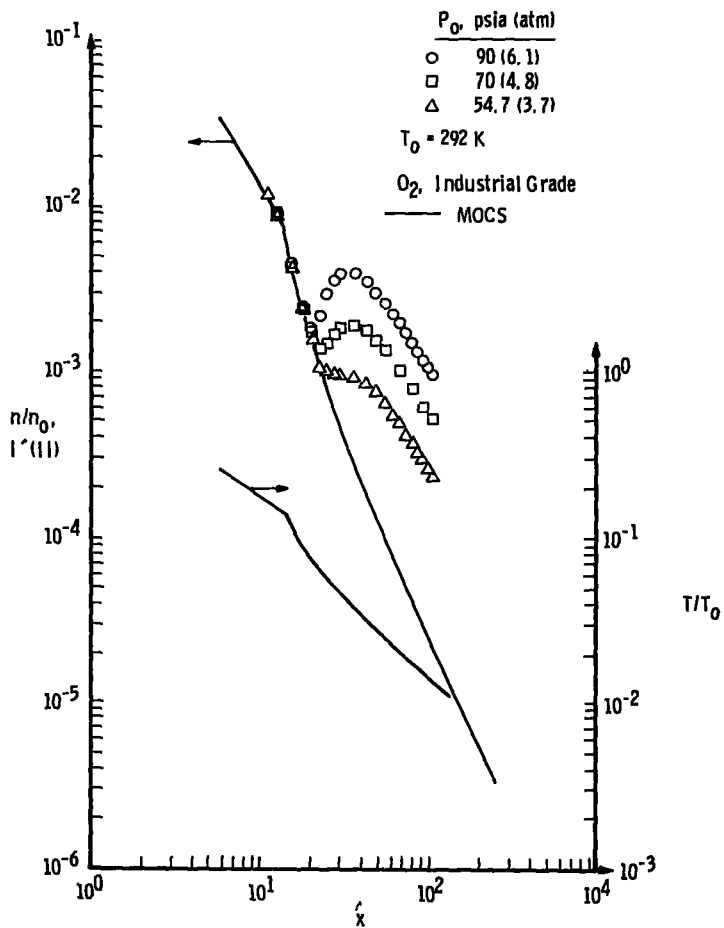


Figure 12. Axial variation of $I'(||)$ for all O_2 reservoir pressures investigated,
 $\theta_{1/2} = 10.5$ deg.

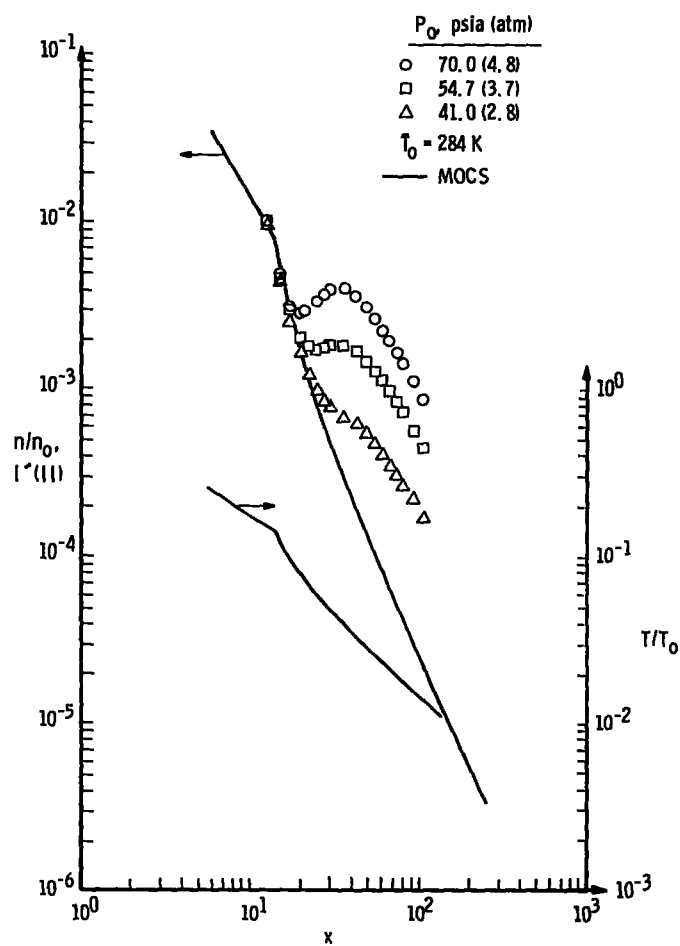


Figure 13. Axial variation of $I'(||)$ for all CO reservoir pressures investigated, $\theta_{12} = 10.5$ deg.

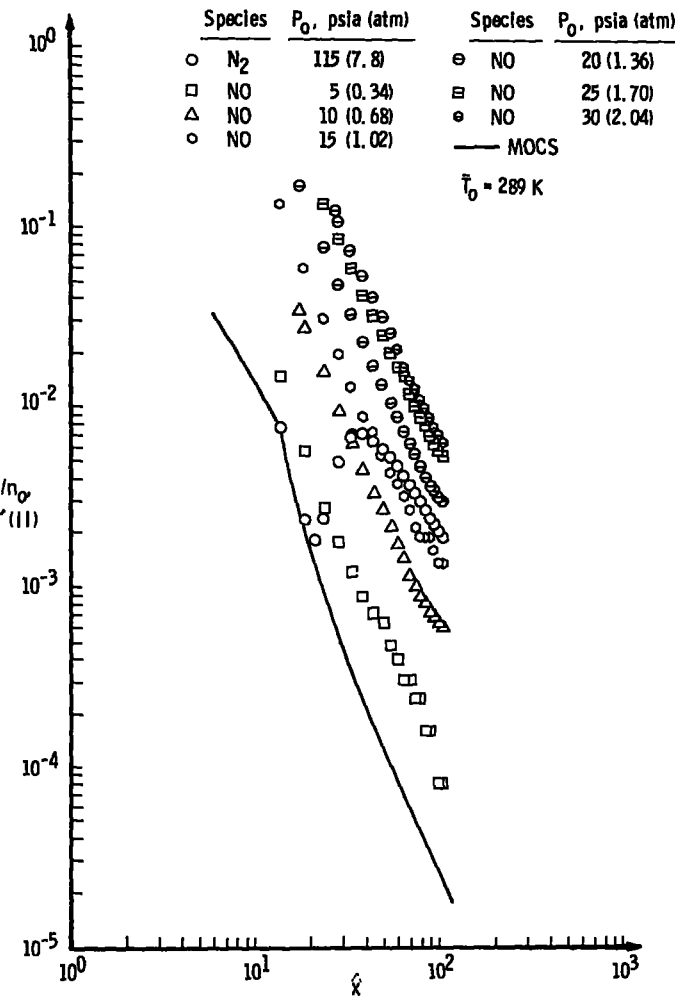


Figure 14. Axial variation of $I'(||)$ for all NO reservoir pressures investigated, $\theta_{12} = 10.5$ deg.

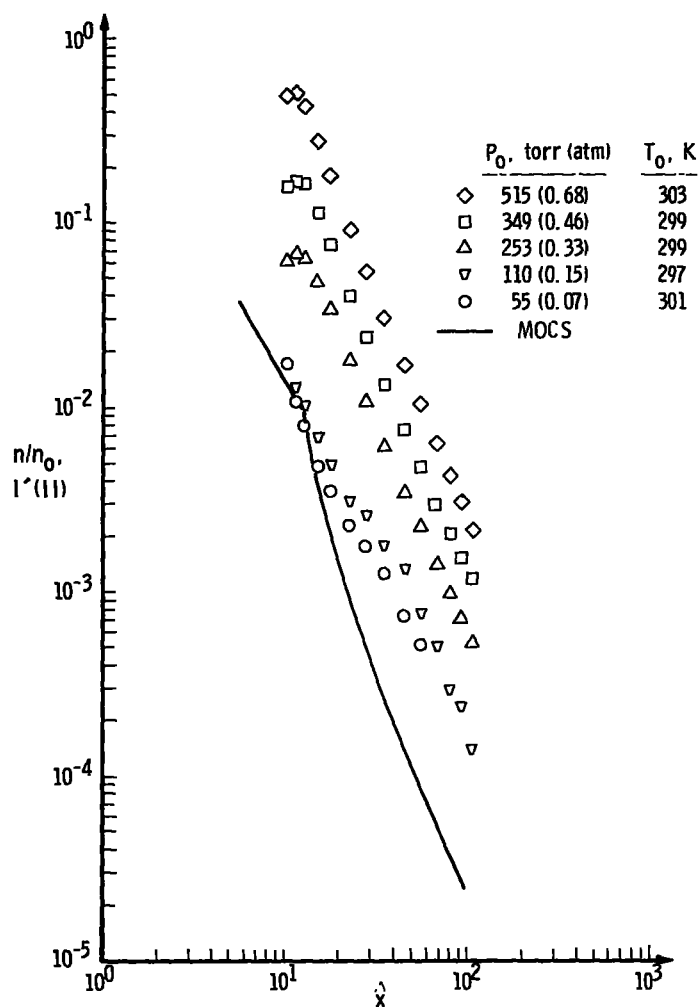


Figure 15. Axial variation of $I'(11)$ for all HCl reservoir pressures investigated, $\theta_{12} = 10.5$ deg.

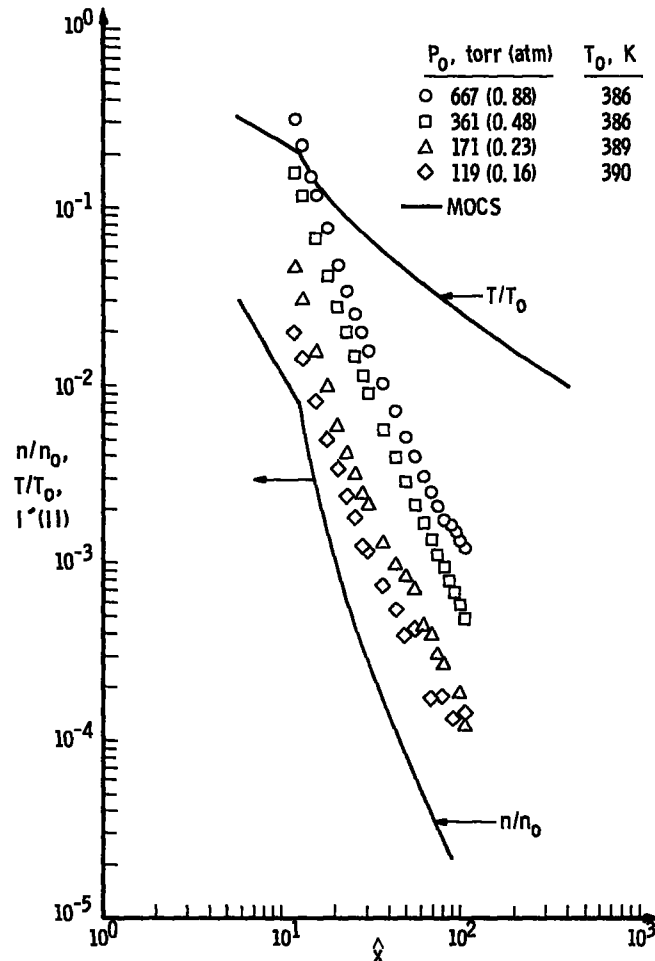
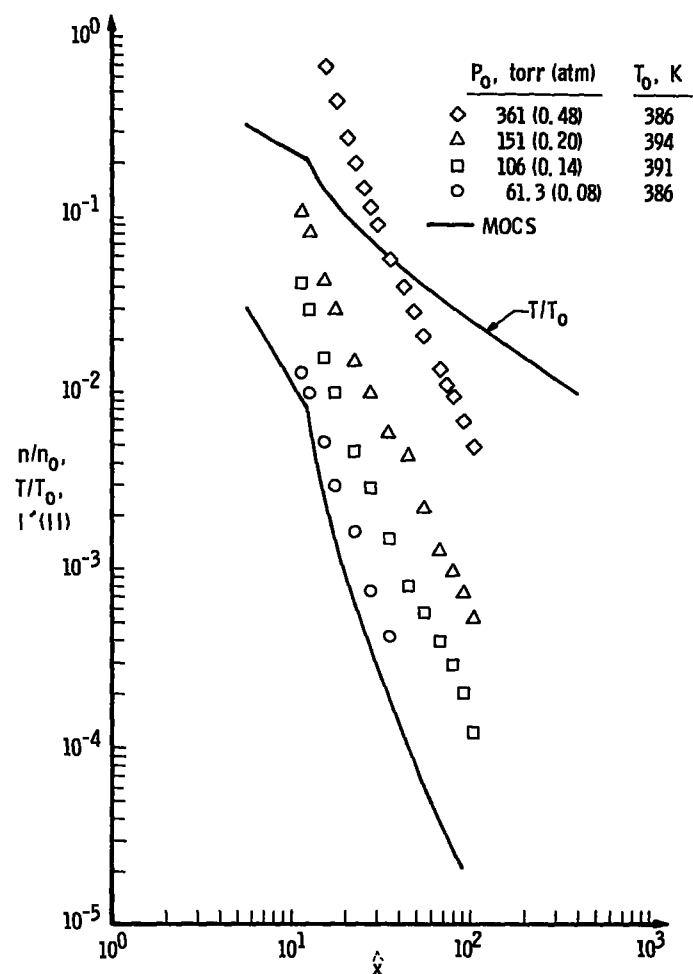


Figure 16. Axial variation of $I'(II)$ for all H_2O reservoir pressures investigated, $\theta_{\text{X}} = 10.5$ deg.

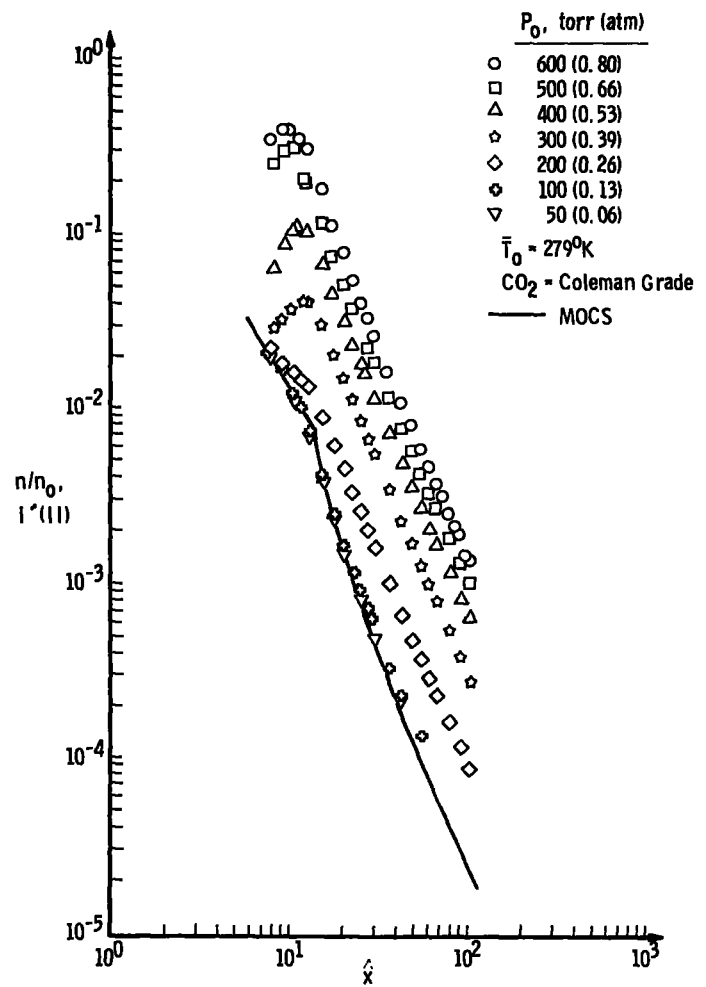


Figure 17. Axial variation of $I'(\parallel)$ for all CO_2 reservoir pressures investigated, $\theta_{\frac{1}{2}} = 10.5$ deg.

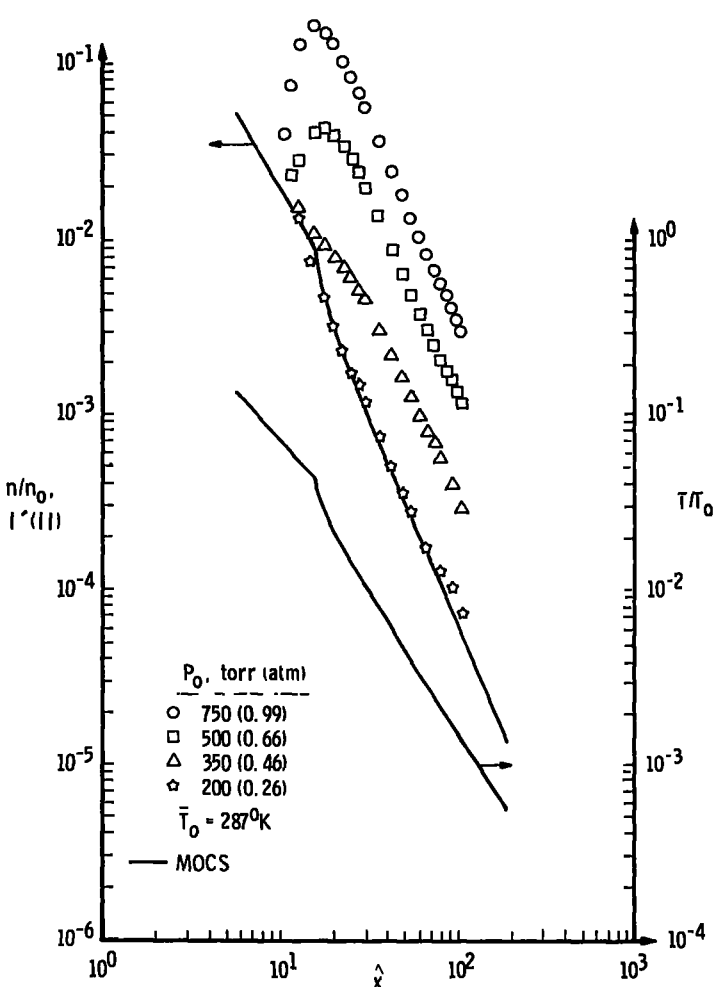


Figure 18. Axial variation of $I'(\parallel)$ for all Ar reservoir pressures investigated, $\theta_{\frac{1}{2}} = 10.5$ deg.

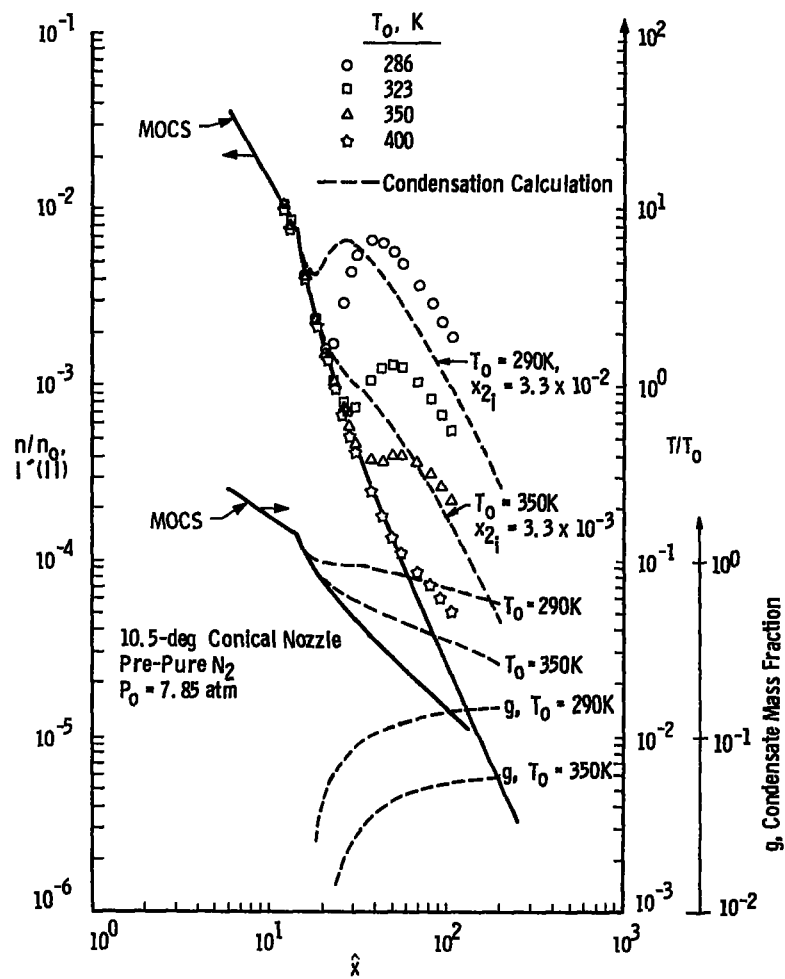


Figure 19. Axial variation of $I'(II)$ for all N_2 reservoir temperatures investigated, $\theta_{\frac{x}{x_2}} = 10.5$ deg.

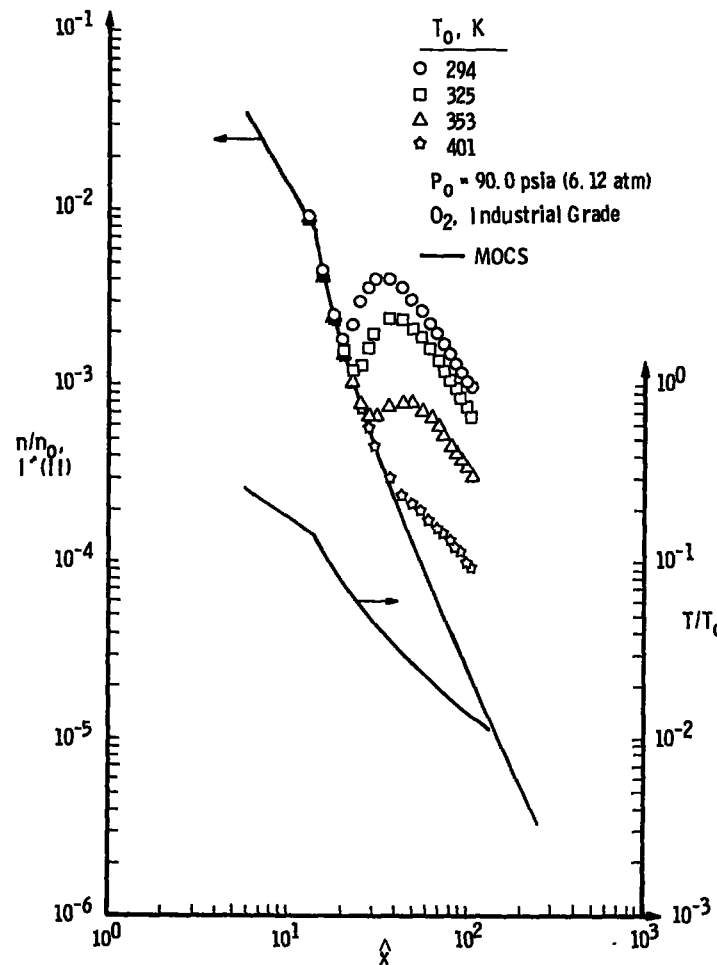


Figure 20. Axial variation of $I'(II)$ for all O_2 reservoir temperatures investigated, $\theta_{\frac{x}{x_2}} = 10.5$ deg.

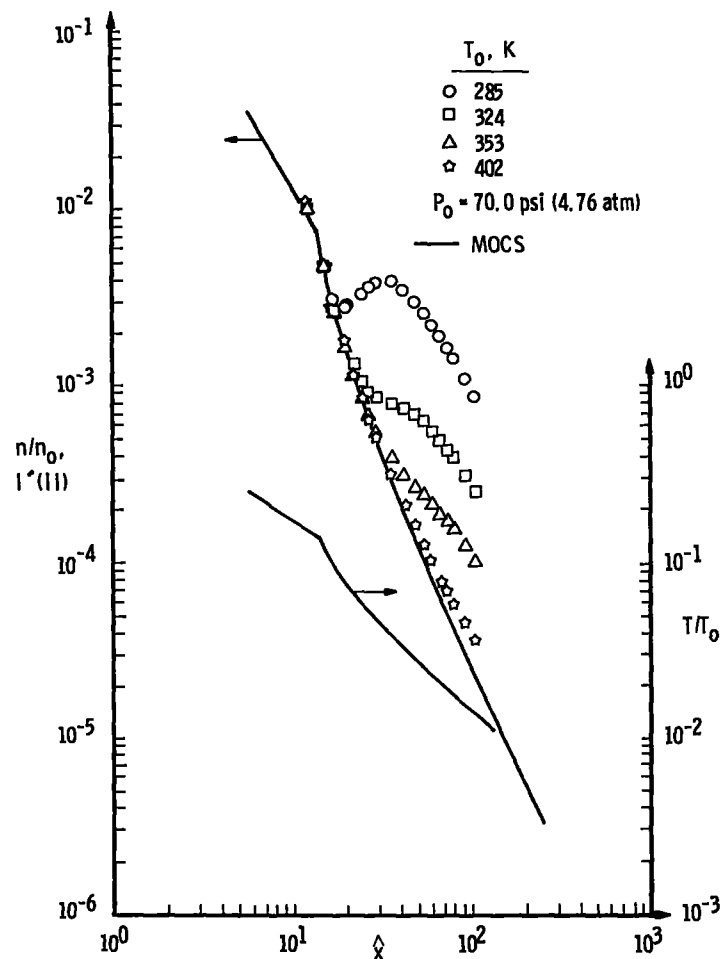


Figure 21. Axial variation of $I'(\parallel)$ for all CO reservoir temperatures investigated, $\theta_{1/2} = 10.5$ deg.

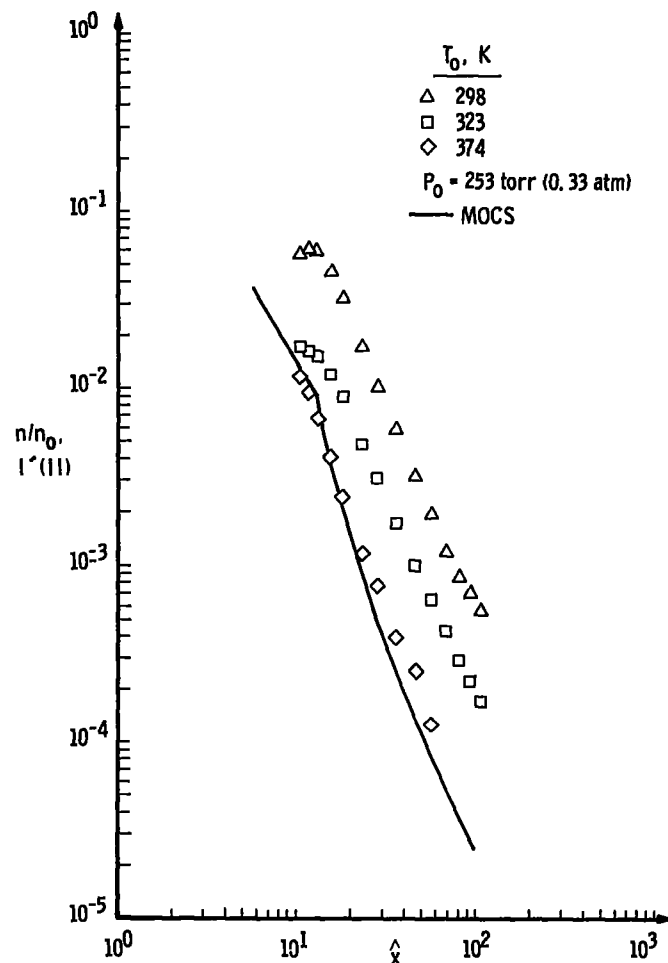


Figure 22. Axial variation of $I'(\parallel)$ for all HCl reservoir temperatures investigated, $\theta_{1/2} = 10.5$ deg.

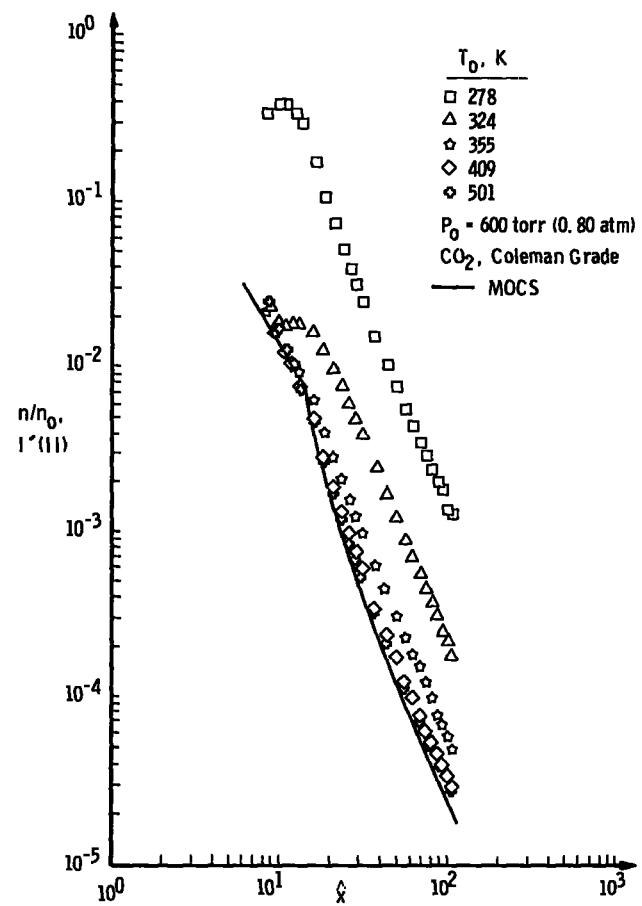


Figure 23. Axial variation of $I'(\parallel)$ for all CO_2 reservoir temperatures investigated, $\theta_{\frac{1}{2}} = 10.5$ deg.

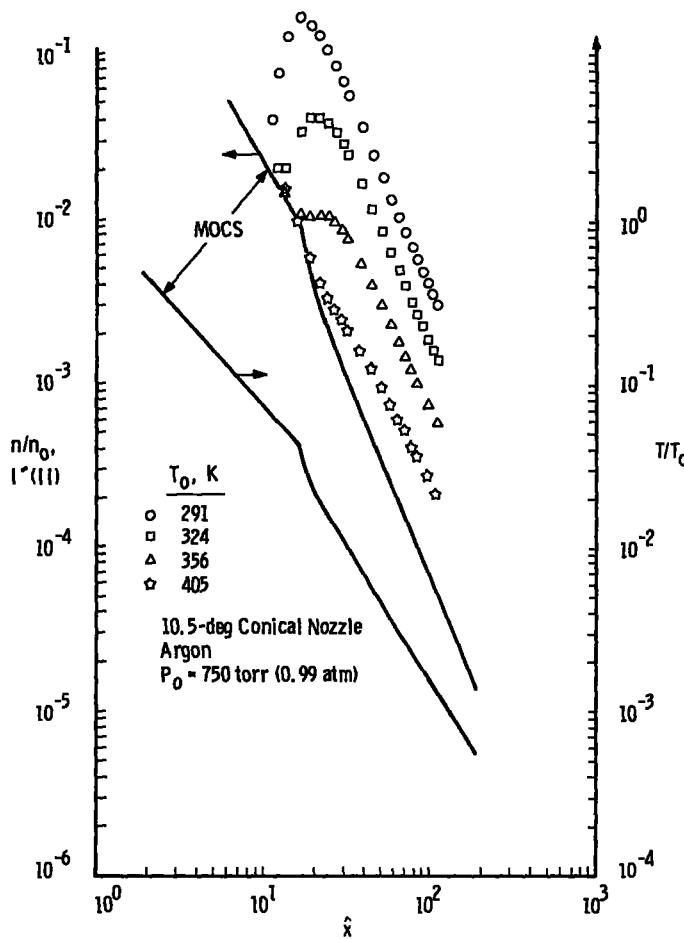


Figure 24. Axial variation of $I'(\parallel)$ for all Ar reservoir temperatures investigated, $\theta_{\frac{1}{2}} = 10.5$ deg.

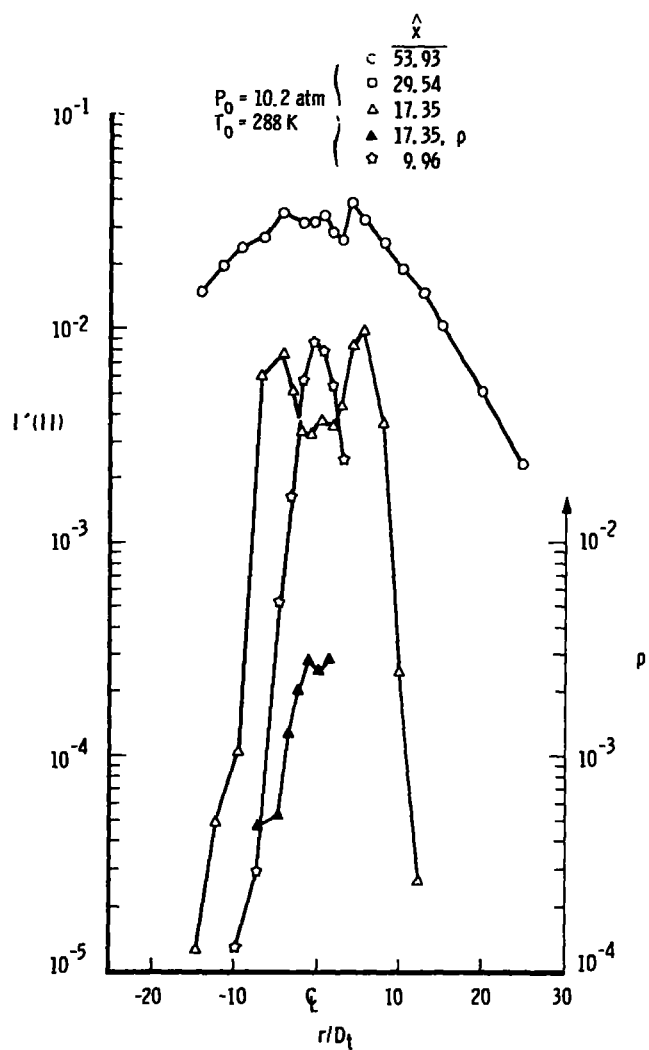


Figure 25. Radial variation of $A'(\text{II})$ for an N_2 reservoir pressure of 10.2 atm at three axial positions, $\theta_{1/2} = 14.5$ deg.

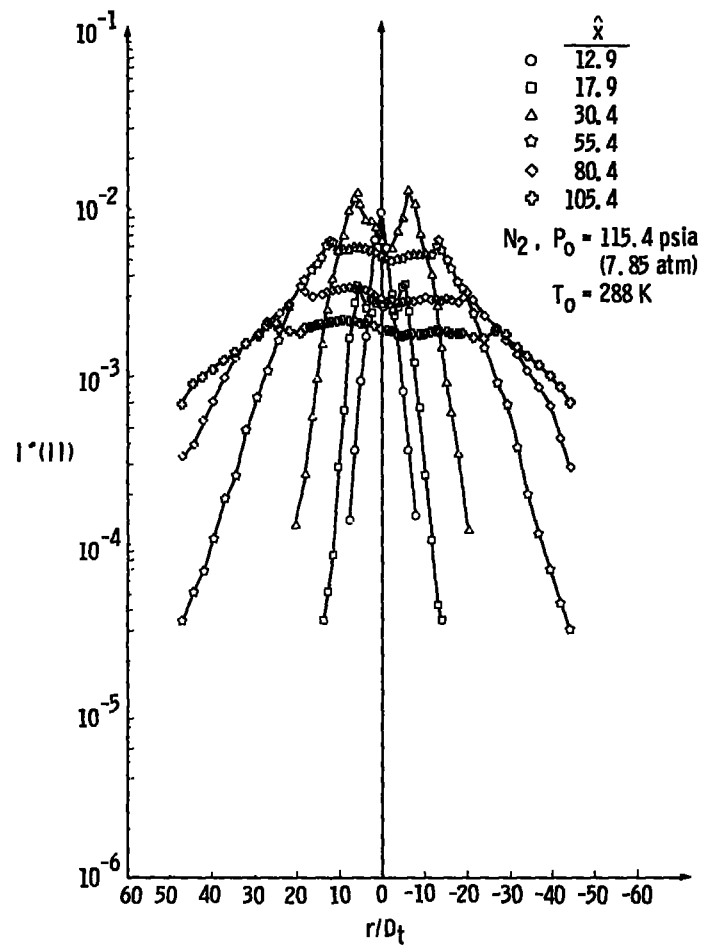


Figure 26. Radial variation of $I'(II)$ for an N_2 reservoir pressure of 7.85 atm at six axial positions, $T_0 = 288 \text{ K}$, $\theta_{12} = 10.5 \text{ deg.}$

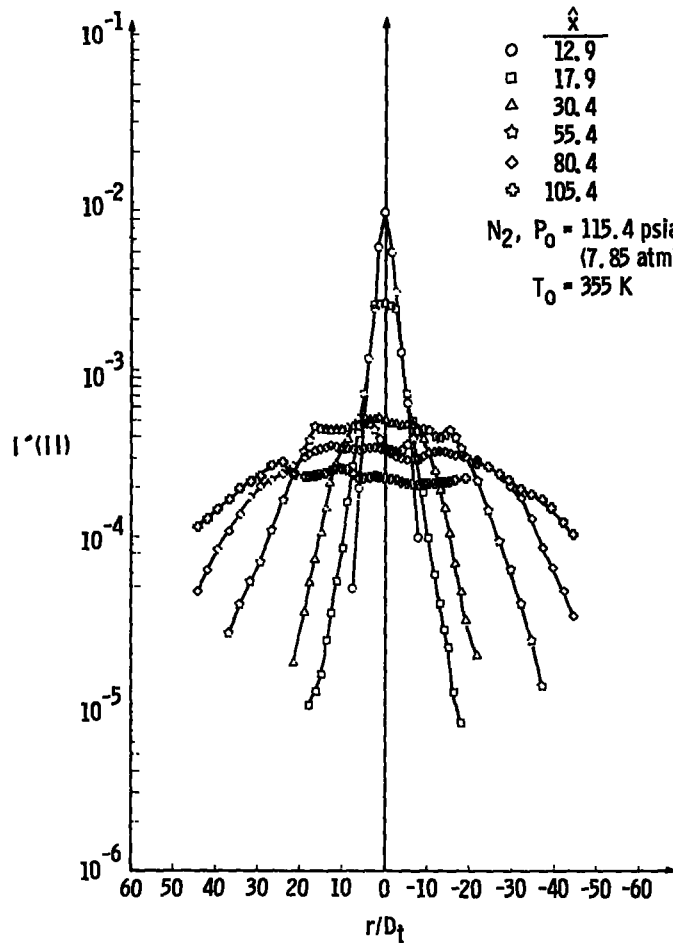


Figure 27. Radial variation of $I'(II)$ for an N_2 reservoir pressure of 7.85 atm at six axial positions, $T_0 = 355 \text{ K}$, $\theta_{12} = 10.5 \text{ deg.}$

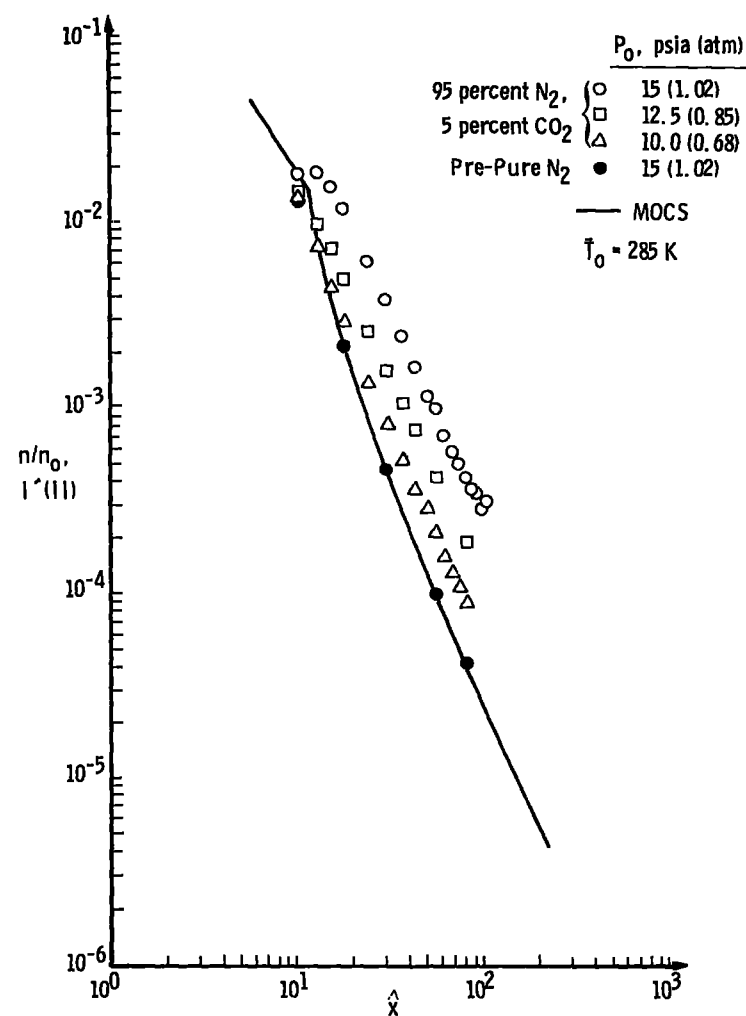


Figure 28. Axial variation of $I'(II)$ for a 95-percent $N_2/5$ -percent CO_2 mixture, $\theta_{1/2} = 9.0$ deg.

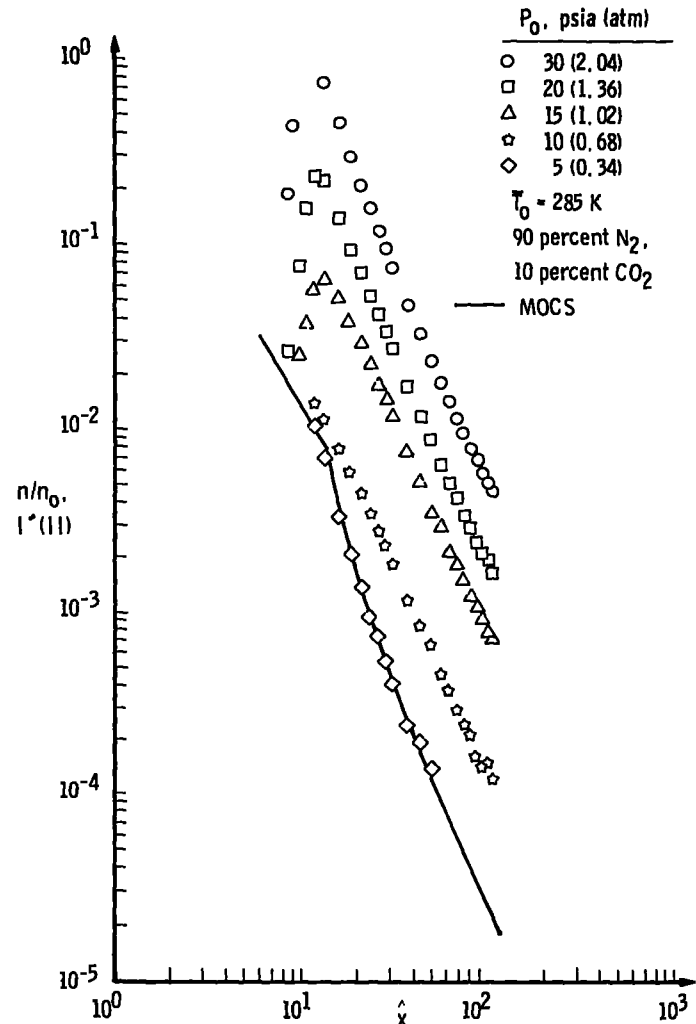


Figure 29. Axial variation of $I'(II)$ for a 90-percent $N_2/10$ -percent CO_2 mixture, $\theta_{1/2} = 10.5$ deg.

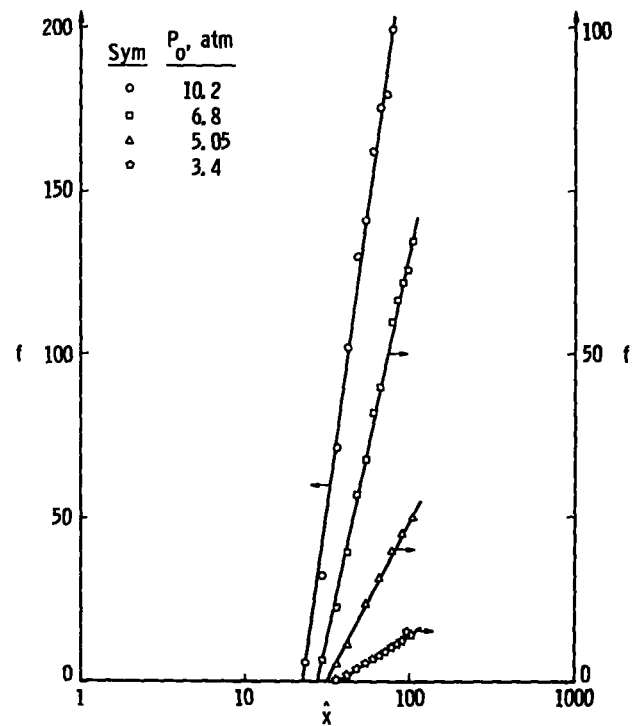


Figure 30. Axial variation of scattering function, f , for 14.5-deg nozzle, N_2 gas, P_0 variation.

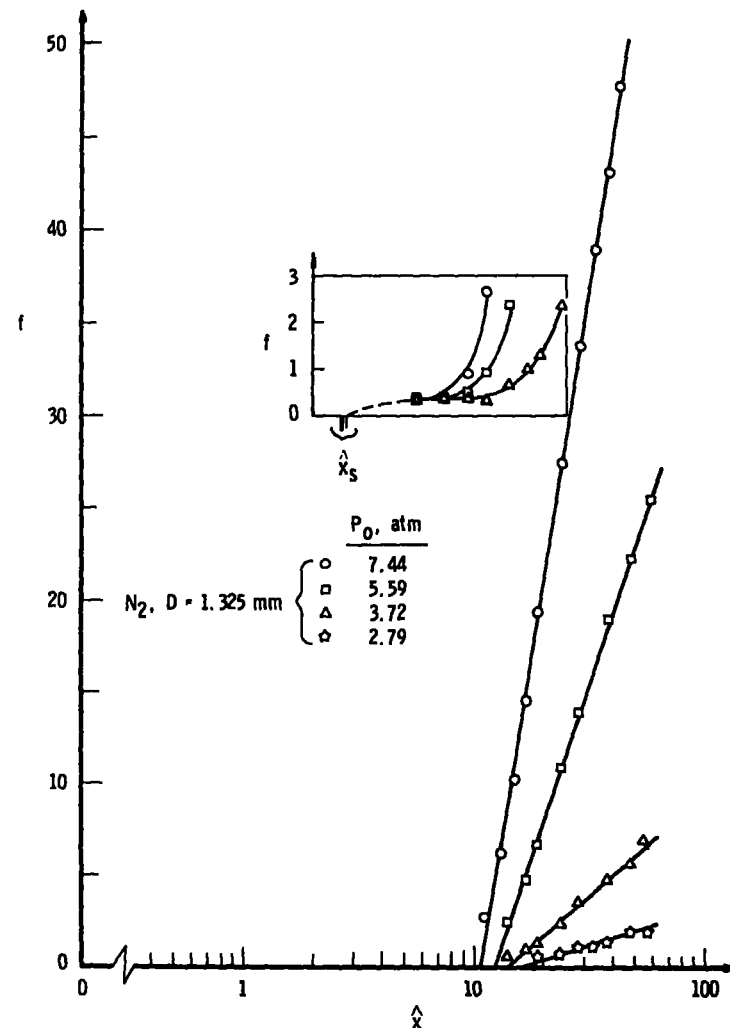


Figure 31. Axial variation of scattering function, f , for sonic orifice, $D = 1.325 \text{ mm}$, N_2 gas.

44

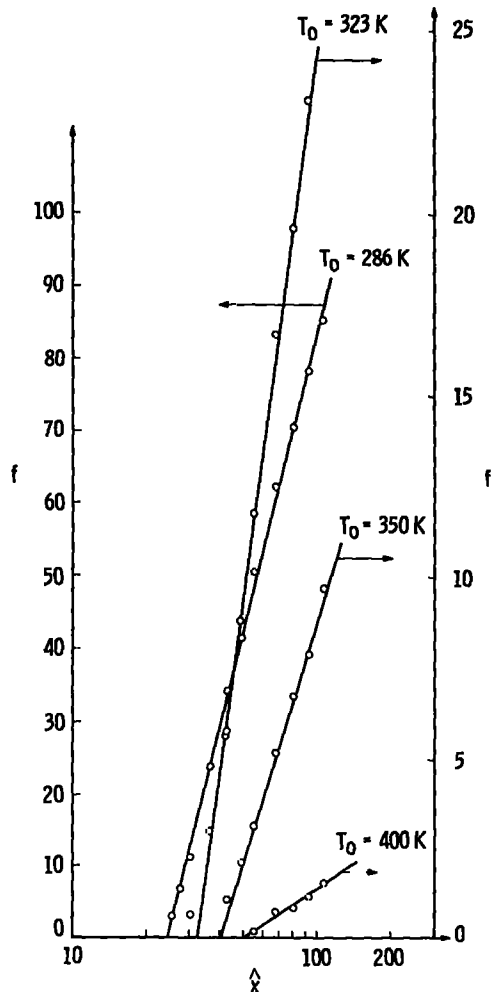


Figure 32. Axial variation of scattering function, f , for 10.5-deg nozzle, N_2 gas, T_0 variation.

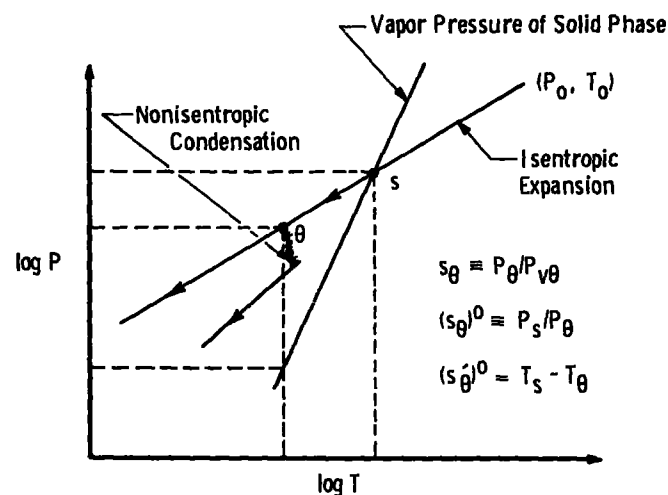


Figure 33. Diagram of expansion process.

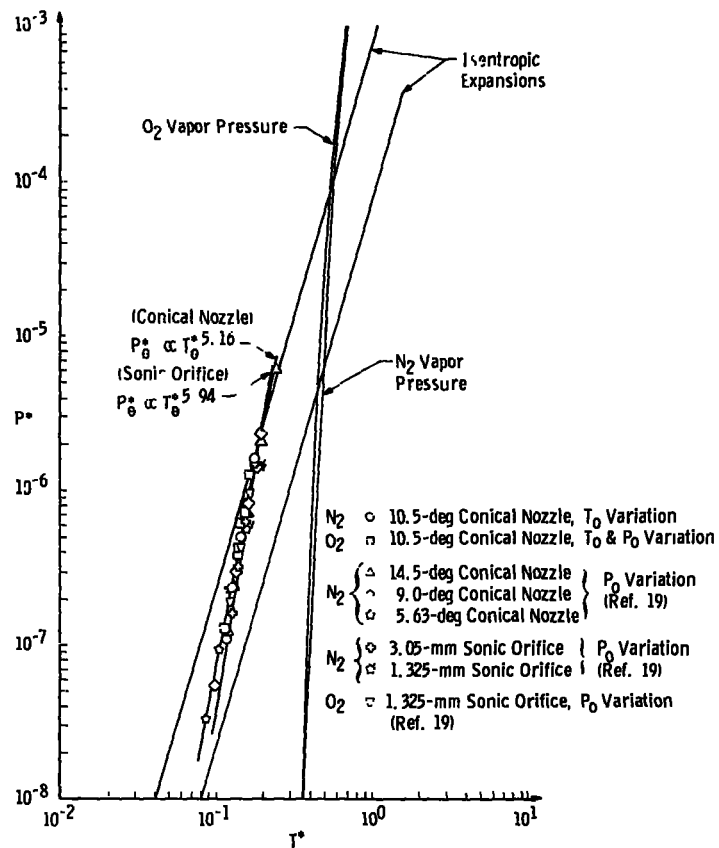


Figure 34. N_2 and O_2 condensation onset locus using reduced values.

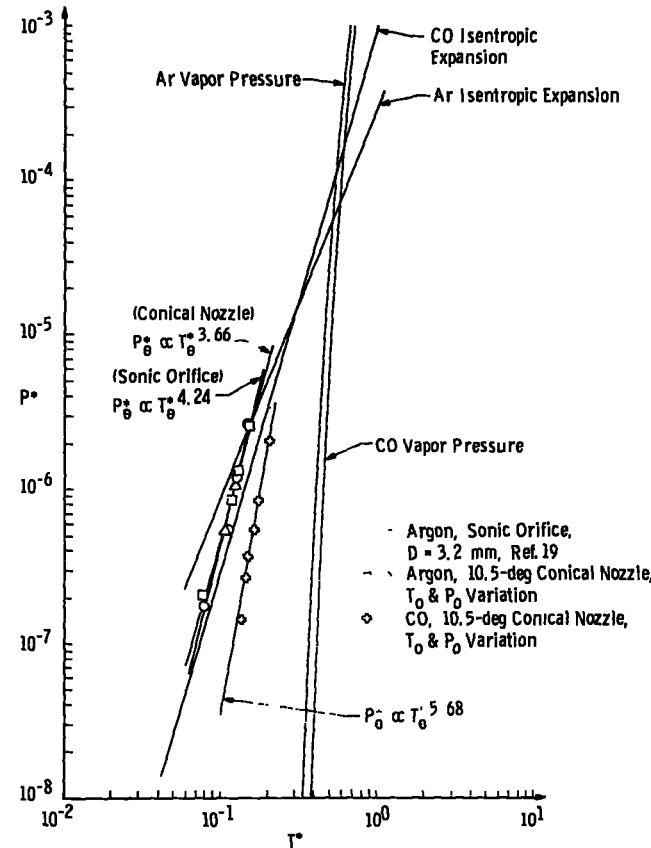


Figure 35. Ar and CO condensation onset locus using reduced values.

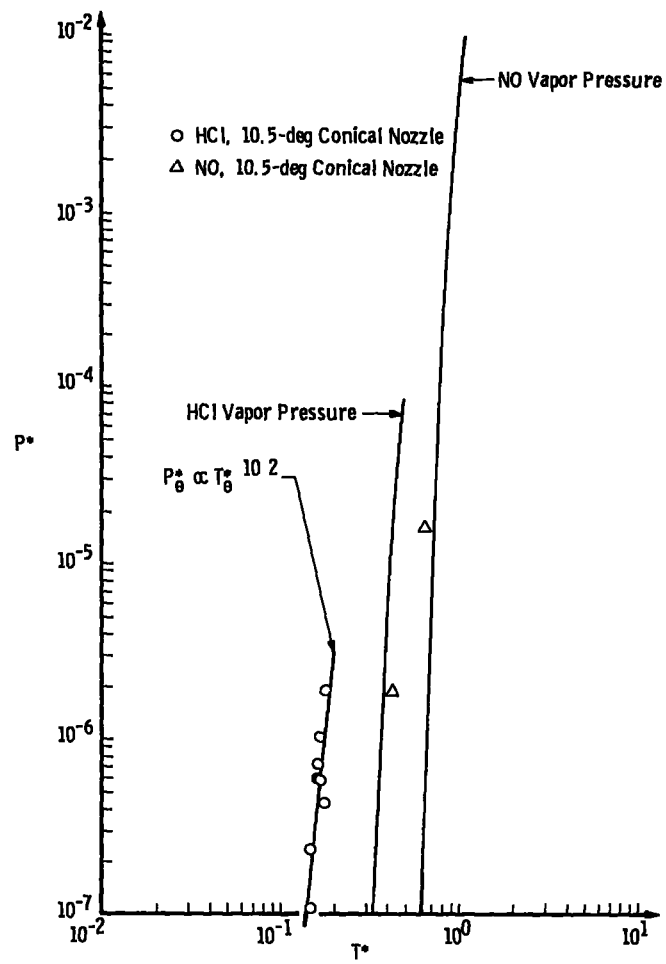


Figure 36. HCl and NO condensation onset locus using reduced values.

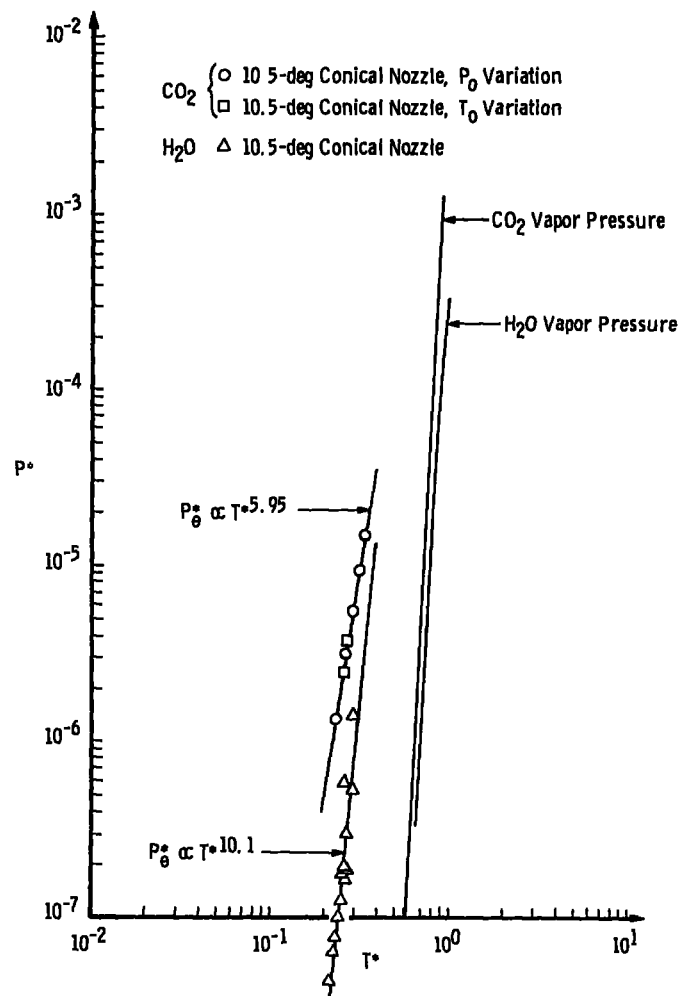


Figure 37. CO_2 and H_2O condensation onset locus using reduced values.

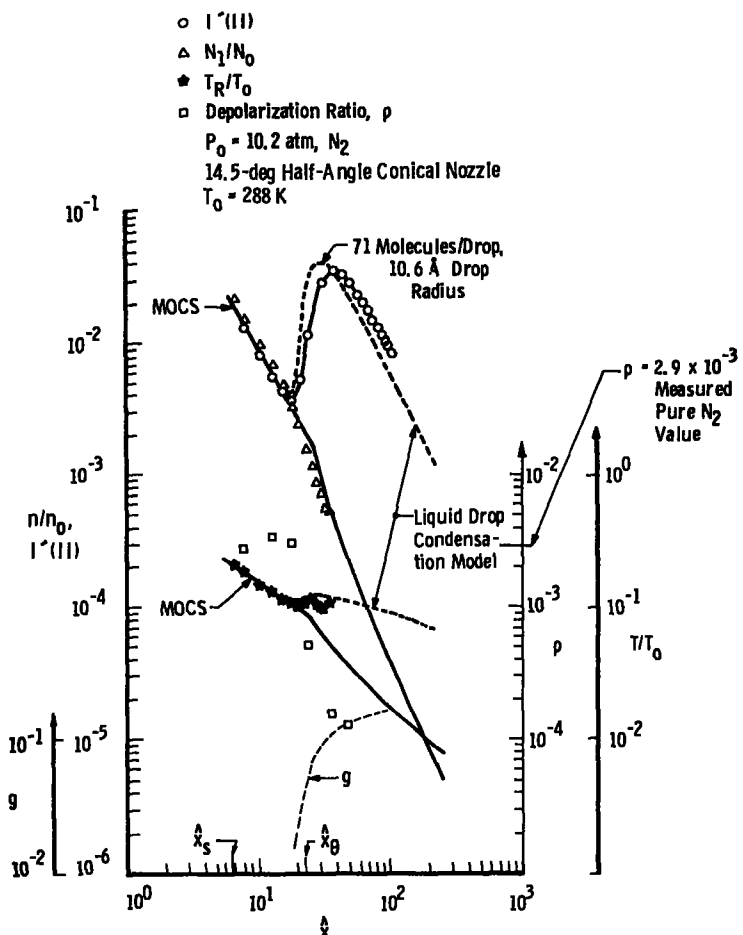


Figure 38. Axial variation of $I'(||)$ number density, temperature, mass fraction (g), and depolarization ratio: 14.5-deg conical nozzle, $P_0 = 10.2$ atm, N_2 .

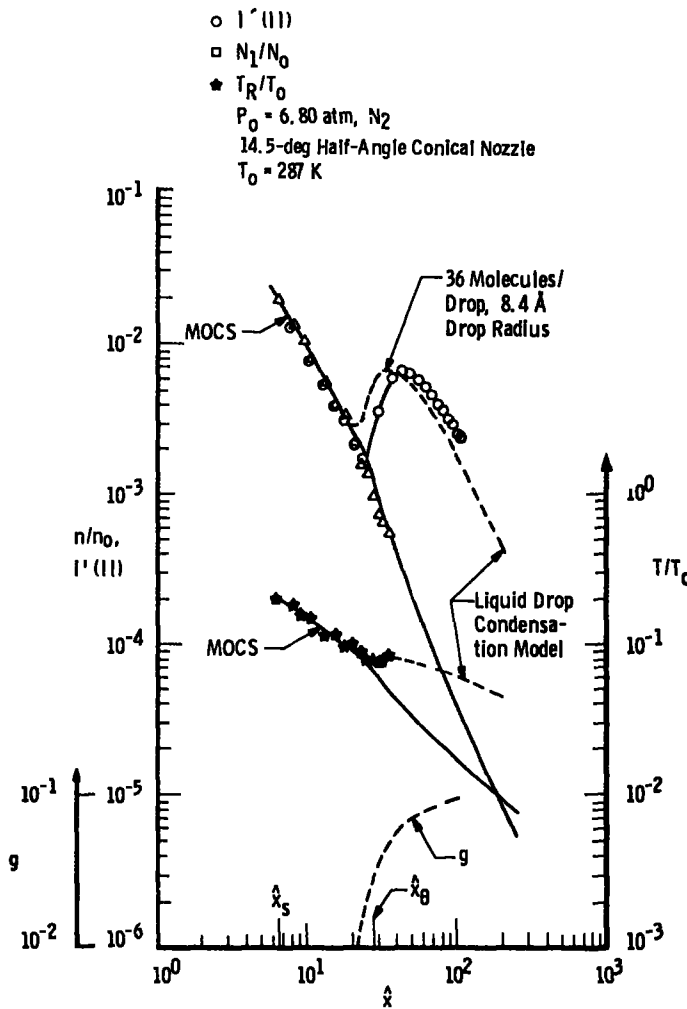


Figure 39. Axial variation of $I'(||)$, number density, temperature, and mass fraction: 14.5-deg conical nozzle, $P_0 = 6.80$ atm, N_2 .

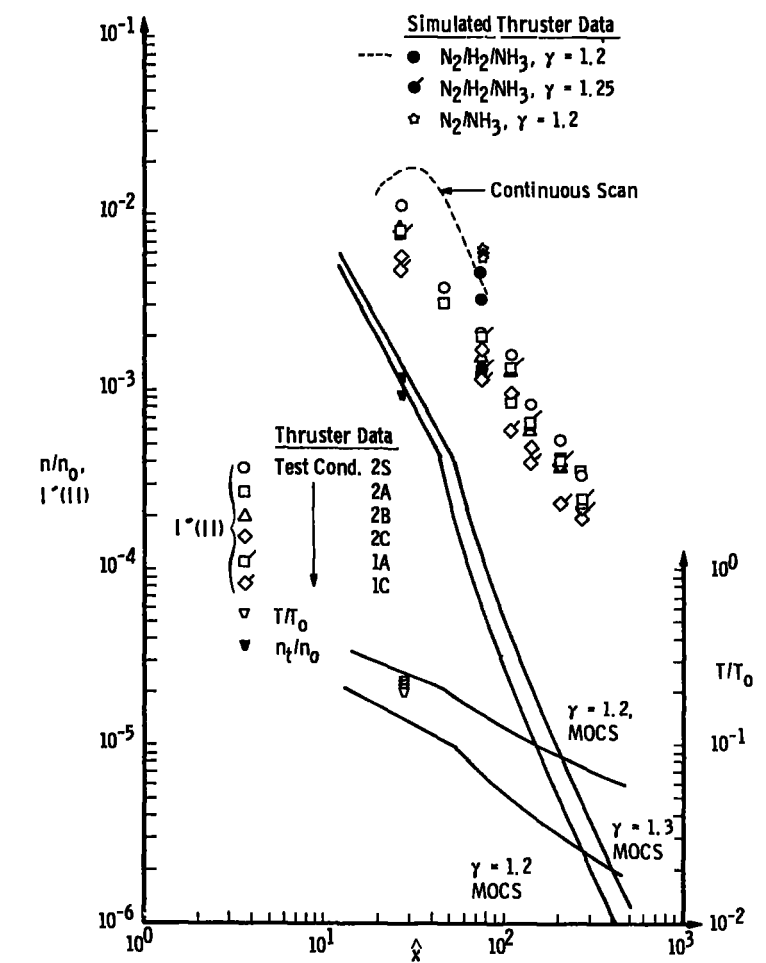


Figure 40. Laser scattering measurements in the new and simulated thruster plumes.

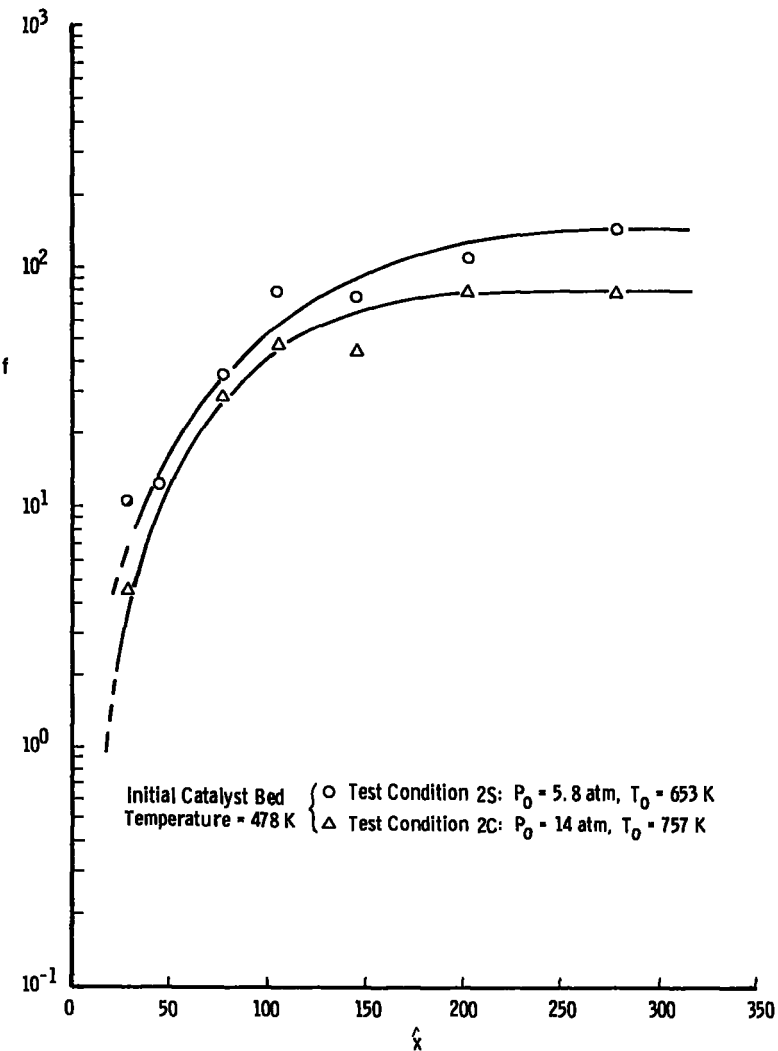


Figure 41. Axial variation of the scattering function, f , in the new thruster plume.

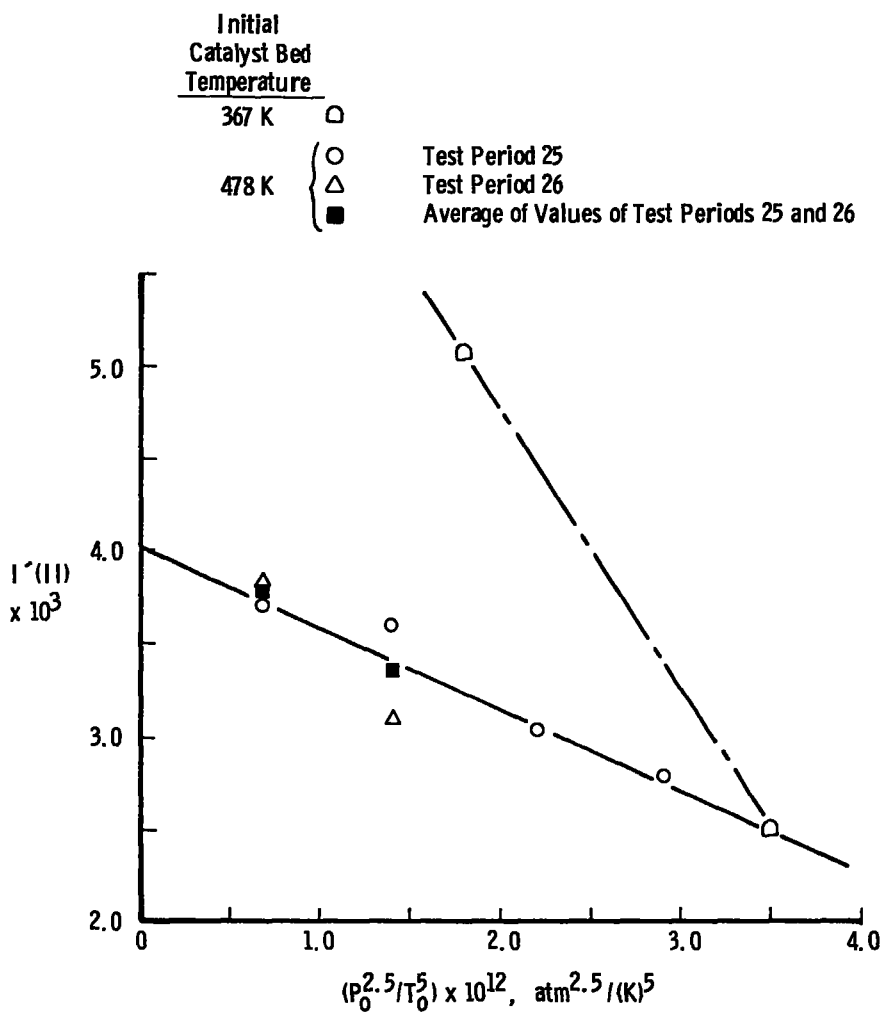


Figure 42. Variation of Rayleigh scattering in the new thruster plume with reservoir parameters at axial position $\hat{x} = 45.2$.

Table 1. Saturation and Condensation Onset Parameters

Gas	$\theta_{1/2}$, deg	D or D_t , mm	T_o , K	P_o , atm	Δ_{X_s}	P_s , torr	T_s , K	Δ_{X_θ}	P_θ , torr	T_θ , K	P_θ^*	T_θ^*	$(s_\theta)^o$	$(s_\theta^*)^o$, K
N_2	N/A	1.325	291	7.44	2.65	20.6	58.0	10.8	0.29	16.9	1.49×10^{-6}	0.178	71.1	41.1
			292	5.59	2.7	12.9	55.5	12.5	0.125	14.9	6.44×10^{-7}	0.157	103.3	40.6
			289	3.72	2.8	7.0	53.0	14.2	0.063	13.3	3.25×10^{-7}	0.140	125.4	39.7
			290	2.79	2.95	4.9	51.0	16.4	0.0314	11.9	1.62×10^{-7}	0.125	156.0	39.1
			285	5.24	2.6	14.6	56.4	9.64	0.274	18.2	1.41×10^{-6}	0.191	53.3	38.2
	5.63	1.00	285	3.95	2.7	9.11	54.0	11.75	0.110	15.1	5.67×10^{-7}	0.159	82.7	38.9
			284	6.19	9.3	16.5	56.0	21.9	0.162	15.1	8.35×10^{-7}	0.159	101.9	40.9
			286	4.13	9.4	9.4	54.0	27.7	0.045	11.7	2.32×10^{-7}	0.123	209.0	42.3
			285	2.97	9.5	5.8	51.0	31.5	0.0176	9.9	9.07×10^{-8}	0.104	329.5	42.1
			283	2.07	9.7	3.6	50.0	39.5	0.0064	8.0	3.30×10^{-8}	0.084	563.0	42.0
9.0	9.0	1.00	285	7.85	9.8	22.5	57.5	22.6	0.459	18.8	2.37×10^{-6}	0.198	49.1	38.7
			283	6.03	10.1	15.5	56.0	24.8	0.275	17.4	1.42×10^{-6}	0.183	56.7	38.6
			286	5.23	10.6	12.8	55.0	27.2	0.16	15.6	8.25×10^{-7}	0.164	81.3	39.4
			287	3.77	12.0	8.0	53.0	31.4	0.0579	12.9	2.98×10^{-7}	0.136	140.0	40.1
			283	2.9	12.2	5.6	51.5	37.0	0.0222	10.6	1.14×10^{-7}	0.112	250.0	40.9
	10.5	1.016	281	2.01	12.4	3.4	49.5	41.0	0.0106	9.5	5.46×10^{-8}	0.0999	323.0	40.0
			286	7.85	8.5	20.8	56.7	24.4	0.309	17.02	1.59×10^{-6}	0.179	67.3	39.7
			323		10.5	12.0	54.7	32.4	0.0990	13.89	5.10×10^{-7}	0.146	121.2	40.8
			350		12.6	8.34	53.2	40.0	0.0461	12.08	2.38×10^{-7}	0.127	180.9	41.1
			400		14.7	4.60	51.3	50.0	0.0211	11.04	1.10×10^{-7}	0.116	218.0	40.3
14.5	1.04		288	10.2	6.3	27.1	58.5	22.4	1.19	23.9	6.13×10^{-6}	0.251	22.7	34.6
			287	6.80	6.6	18.3	56.8	27.6	0.40	19.1	2.06×10^{-6}	0.201	45.5	37.5
			286	5.05	7.1	11.3	54.8	31.5	0.138	15.4	7.11×10^{-7}	0.162	81.9	39.4
			284	3.40	7.4	7.0	52.8	37.8	0.046	12.5	2.37×10^{-7}	0.132	152.2	40.3
			285	2.66	7.9	4.85	51.0	42.0	0.0235	11.2	1.21×10^{-7}	0.118	206.0	40.1
			285	1.93	8.3	3.1	49.4	---	---	---	---	---	---	---

Table 1. Continued

Gas	$\theta_{1/2}^*$, deg	D or D_t , mm	T_o , K	P_o , atm	Δ_{X_s}	P_s , torr	T_s , K	Δ_{X_θ}	P_θ , torr	T_θ , K	P_{θ}^*	T_{θ}^*	$(s_\theta)^*$, °	(s_θ') , K
O_2	N/A	1.325	283	3.72	2.24	16.6	65.0	8.65	0.256	19.8	9.66×10^{-7}	0.169	64.8	45.2
			285	2.79	2.31	11.1	63.5	10.3	0.116	17.2	4.38×10^{-7}	0.146	95.7	46.3
			283	1.85	2.38	8.18	61.4	12.5	0.051	14.4	1.92×10^{-7}	0.123	160.5	47.0
			281	1.0	2.55	3.05	58.0	—	—	—	—	—	—	—
			10.5	1.016	294	6.12	7.1	25.7	66.2	22.6	0.338×10^{-6}	0.165	76.0	46.8
	↓	↓	325	—	8.4	16.8	64.6	25.4	0.193	18.2	7.27×10^{-7}	0.155	87.0	46.4
			353	—	10.0	11.1	62.6	30.3	0.101	16.6	3.81×10^{-7}	0.141	109.9	46.0
			401	—	12.6	6.33	60.5	40.8	0.0343	13.4	1.29×10^{-7}	0.114	184.5	47.1
			291	4.76	7.1	19.2	65.2	24.8	0.168	16.9	6.34×10^{-7}	0.144	114.3	48.3
			291	3.72	7.3	14.3	63.8	25.7	0.112	16.2	4.23×10^{-7}	0.138	127.7	47.6
CO	N/A	1.325	291	3.72	2.65	9.4	58.0	5.75	0.81	29.1	—	—	11.6	28.9
			284	2.79	2.6	7.7	57.5	5.96	0.57	27.5	—	—	13.5	30.0
			285	1.31	2.79	3.2	54.0	6.05	0.147	27.2	—	—	21.8	26.8
			283	0.66	2.9	1.38	52.0	—	—	—	—	—	—	—
			283	0.26	3.1	0.46	49.0	—	—	—	—	—	—	—
	↓	↓	285	4.76	7.9	14.9	59.3	20.5	0.402	21.1	2.07×10^{-6}	0.211	37.1	38.2
			324	—	10.0	8.69	57.4	27.8	0.107	16.5	5.52×10^{-7}	0.165	81.2	40.9
			353	—	11.7	5.70	56.1	33.6	0.0525	14.8	2.71×10^{-7}	0.148	108.6	41.3
			402	—	14.4	3.24	54.1	40.0	0.0279	13.9	1.44×10^{-7}	0.139	116.1	40.2
			283	3.72	8.0	11.5	58.3	23.5	0.167	17.5	8.61×10^{-7}	0.175	68.9	40.8

Table 1. Continued

Gas	$\theta_{1/2}$, deg	D or D _t , mm	T _o , K	P _o , atm	Δ_{X_B}	P _s , torr	T _s , K	Δ_{X_θ}	P _θ , torr	T _θ , K	P _θ [*]	T _θ [*]	(s _θ)°	(s' _θ)°, K		
Ar	N/A	3.20	280	0.987	1.18	19.5	64.0	3.14	0.84	18.2	2.68×10^{-6}	0.152	23.2	45.8		
			281	0.658	1.20	12.0	62.0	3.56	0.375	15.5	1.19×10^{-6}	0.129	30.9	46.5		
			277	0.461	1.22	8.0	60.0	3.88	0.176	13.6	5.61×10^{-7}	0.114	43.9	46.4		
			275	0.329	1.24	5.6	59.0	4.95	0.056	9.56	1.78×10^{-7}	0.0798	96.5	49.4		
			276	0.263	1.25	4.25	---	---	---	---	---	---	---	---		
	10.5	1.016	291	0.987	0.37	17.3	63.5	11.0	0.816	18.6	2.6×10^{-6}	0.155	21.2	44.9		
			324	---	0.41	12.2	62.3	13.8	0.415	15.7	1.32×10^{-6}	0.131	29.4	46.6		
			356	---	0.45	9.36	61.1	15.9	0.270	14.2	8.6×10^{-7}	0.119	34.7	46.9		
			405	---	0.48	6.34	59.9	19.0	0.0656	9.32	2.09×10^{-7}	0.0778	96.6	50.6		
			288	0.658	0.37	10.8	62.1	13.1	0.333	14.9	1.06×10^{-6}	0.124	32.4	47.2		
	\downarrow	286	0.461	0.38	7.13	60.1	14.6	0.169	13.2	5.38	$\times 10^{-7}$	0.110	42.2	46.9		
\downarrow			279	0.789	1.55	112.14	173.2	6.1	4.74	69.22	1.50×10^{-5}	0.338	23.66	103.98		
			0.658	1.58	89.96	171.2	6.9	2.97	64.17	9.43×10^{-6}	0.313	30.12	107.03			
			0.526	1.63	68.67	168.1	7.76	1.79	59.43	5.68×10^{-6}	0.29	38.36	108.67			
			0.395	1.65	48.83	165.4	8.72	1.01	54.13	3.21×10^{-6}	0.264	48.35	111.27			
			0.263	1.73	29.61	161.3	10.4	0.425	47.43	1.35×10^{-6}	0.231	69.67	113.87			
			0.132	1.83	12.92	155.8	---	---	---	---	---	---	---			
			0.066	1.95	5.64	149.0	---	---	---	---	---	---	---			
			324	0.789	2.05	60.17	167.9	10.8	1.2	54.43	3.81×10^{-6}	0.266	50.14	113.47		
			355	0.789	2.43	40.95	164.0	13.0	0.784	52.9	2.49×10^{-6}	0.258	52.23	111.1		
			301	0.072	1.86	2.66	127	11.4	0.0975	48.8	1.09×10^{-7}	0.149	27.3	78.2		
HCl	10.5	1.016	297	0.145	1.60	7.0	134	11.2	0.210	49.3	2.35×10^{-7}	0.150	33.3	84.7		
			299	0.333	1.33	19.3	142	9.8	0.650	53.82	7.26×10^{-7}	0.164	29.7	88.2		
			299	0.459	1.25	28.6	145	9.7	0.922	54.12	1.03×10^{-6}	0.165	31.0	90.9		
			303	0.678	1.13	44.0	149	8.8	1.72	58.8	1.92×10^{-6}	0.179	25.6	90.2		
			298	0.333	1.33	19.3	142	10.1	0.539	53.34	6.02×10^{-7}	0.163	35.8	88.7		
			323	---	1.42	13.5	139	10.8	0.525	54.91	5.86×10^{-7}	0.167	25.7	84.1		
			374	---	1.60	7.0	134	12.2	0.395	58.34	4.41×10^{-7}	0.178	17.7	75.7		

Table 1. Concluded

Gas	$\theta_{1/2}$, deg	D or D_t , mm	T_o , K	P_o , atm	\hat{X}_s	P_s , torr	T_s , K	\hat{X}_θ	P_θ , torr	T_θ , K	P_θ^*	T_θ^*	(s_θ) , °	(s_θ) , K	
NO	10.5	1.016	289	0.340	4.25	4.7	92	9.05	0.805	54.9	1.89×10^{-6}	0.419	5.84	37.1	
				0.680	4.0	10.7	95	4.89	6.9	83.8	1.62×10^{-5}	0.64	1.55	11.2	
				1.02	3.9	17.8	97.5	—	—	—	—	—	—	—	
				1.36	3.8	24.6	99	—	—	—	—	—	—	—	
				1.70	3.75	31.0	100	—	—	—	—	—	—	—	
H_2O	10.5	1.016	390	0.071	0.178	16.9	290	12.2	0.0902	81.5	4.28×10^{-8}	0.215	187.4	208.5	
				384	0.137	<0.08	43.5	309	8.7	0.371	95.6	1.76×10^{-7}	0.252	117.3	213.4
				394	0.199	<0.08	61.5	315	8.0	0.647	102.8	3.07×10^{-7}	0.271	95.1	212.2
				391	0.139	<0.08	41.0	308	8.4	0.418	99.7	1.98×10^{-7}	0.262	98.1	208.3
				386	0.081	0.146	21.0	295	10.8	0.137	85.7	6.49×10^{-8}	0.226	153.3	209.3
				388	0.678	<0.08	360	354	7.0	3.03	108.6	1.44×10^{-6}	0.286	118.8	245.4
				409	0.138	0.109	31.0	301	8.5	0.395	102.7	1.87×10^{-7}	0.270	78.5	198.3
				407	0.130	0.115	29.5	300	8.8	0.343	100.9	1.63×10^{-7}	0.266	86.0	199.1
				404	0.121	0.115	28.2	300	9.5	0.269	96.2	1.28×10^{-7}	0.253	104.8	203.8
				404	0.114	0.129	25.5	298	10.3	0.215	92.9	1.02×10^{-7}	0.245	118.6	205.1
				405	0.107	0.141	23.5	296	11.2	0.167	88.7	7.93×10^{-8}	0.233	140.7	207.3
				386	0.878	<0.08	525	363	7.3	3.52	105.4	1.67×10^{-6}	0.277	149.1	257.6
				386	0.475	<0.08	220	342	8.7	1.29	96.1	6.11×10^{-7}	0.253	170.5	245.9
				389	0.225	<0.08	78.0	320	6.6	1.19	112.8	5.43×10^{-7}	0.297	65.5	207.2
				390	0.157	<0.08	45.1	309	8.9	0.407	96.3	1.93×10^{-7}	0.254	110.8	212.7

Table 2. Sonic Orifice Scaling Constants

Gas	D, mm	m_o	m_2	m_3
N_2	1.325	2.94	1.84	0.25
N_2	3.050	2.93	1.84	0.25
O_2	1.325	2.98	2.05	---
CO	1.325	2.87	---	---
Ar	3.200	3.03	1.96	---

Table 3. Conical Nozzle Scaling Constants

Gas	D_t , mm	$\theta_{1/2}$, deg	m_o	m_1	m_2	m_3	m_4
N_2	1.04	14.5	---	---	---	---	---
N_2	1.00	9.0	2.98	---	2.10	0.25	---
N_2	1.00	5.63	---	---	---	---	---
N_2	1.016	10.5	---	9.59	---	---	2.12
O_2			2.98	9.33	1.06	---	2.03
Ar			3.21	11.0	1.73	---	1.6
CO			2.87	10.5	1.95	---	1.97
CO_2			2.8	13.6	1.73	---	2.75
HCl			2.67	15.4	0.48	---	0.83
H_2O			2.69	---	0.64	---	---
NO			2.46	---	---	---	---

Table 4. Lennard-Jones 12-6 Intermolecular Potential Constants

Gas	$T' = \epsilon/k$, K	ϵ , ergs	$D' = \sigma$, cm	$p' = \epsilon/\sigma^3$, torr
N_2	95.05	1.31×10^{-14}	3.70×10^{-8}	1.94×10^5
O_2	117.50	1.62×10^{-14}	3.58×10^{-8}	2.65×10^5
CO	100.20	1.38×10^{-14}	3.76×10^{-8}	1.94×10^5
CO_2	205.00	2.83×10^{-14}	4.07×10^{-8}	3.15×10^5
Ar	119.80	1.65×10^{-14}	3.40×10^{-8}	3.14×10^5
NO	131.00	1.81×10^{-14}	3.17×10^{-8}	4.26×10^5
HCl	328.00	4.53×10^{-14}	3.36×10^{-8}	8.96×10^5
H_2O	380.00	5.24×10^{-14}	2.65×10^{-8}	2.11×10^6

Table 5. Comparison of Rayleigh Scattering Data for the Aged, New, and Simulated Thruster Plumes

Plume	Test Condition	$I'(\parallel)$	MOCS $n/n_o, \gamma = 1.2$	MOCS $n/n_o, \gamma = 1.3$	$f (\gamma = 1.2)$	\hat{x}
Aged Thruster	2S	1.04×10^{-1}	5.40×10^{-5}	1.1×10^{-4}	1.92×10^3	78.5
New Thruster	2S	2.08×10^{-3}			3.75×10^1	78.5
Simulated Thruster, $\gamma = 1.2$	2S, N_2-NH_3	6.06×10^{-3}			1.11×10^2	
Simulated Thruster, $\gamma = 1.2$	2S, $N_2-NH_3-H_2$	3.94×10^{-3}			7.19×10^1	
Simulated Thruster, $\gamma = 1.25$	2S, $N_2-NH_3-H_2$	1.29×10^{-3}	↓	↓	2.29×10^1	↓
Aged Thruster	2A	4.06×10^{-1}	1.03×10^{-3}	1.3×10^{-3}	3.93×10^2	28.5
New Thruster	2A	8.14×10^{-3}	1.03×10^{-3}	1.3×10^{-3}	6.90	28.5

**Table 6. Rayleigh Scattering Intensity, New Thruster Plume,
Test Period No. 25, $\hat{x} = 45.2$**

Test Condition	$I'(1)$	T_o, K	n_o, cm^{-3}	$\gamma = 1.2$ n/n_o
2S	3.71×10^{-3}	653	7.00×10^{19}	4.3×10^{-4}
2A	3.61×10^{-3}	710	9.67×10^{19}	
2B	3.04×10^{-3}	739	1.186×10^{20}	
2C	2.78×10^{-3}	757	1.326×10^{20}	
1A	5.07×10^{-3}	679	1.013×10^{20}	
1C	2.49×10^{-3}	730	1.372×10^{20}	

**Table 7. Rayleigh Scattering Intensity, New Thruster Plume,
Test Period No. 26**

\hat{x}	Test Condition 2S	Test Condition 2A	Test Condition 2B	Test Condition 2C	Test Condition 1A	Test Condition 1C
278.5	3.35×10^{-4}	3.55×10^{-4}	2.32×10^{-4}	1.96×10^{-4}	2.48×10^{-4}	2.17×10^{-4}
211.8	5.34×10^{-4}	4.12×10^{-4}	3.71×10^{-4}	3.80×10^{-4}	4.11×10^{-4}	2.35×10^{-4}
145.2	8.29×10^{-4}	6.38×10^{-4}	5.97×10^{-4}	4.81×10^{-4}	6.51×10^{-4}	3.95×10^{-4}
111.8	1.57×10^{-3}	8.47×10^{-4}	1.26×10^{-3}	9.67×10^{-4}	1.28×10^{-3}	5.95×10^{-4}
78.5	2.08×10^{-3}	1.21×10^{-3}	1.50×10^{-3}	1.68×10^{-3}	1.99×10^{-3}	1.17×10^{-3}
45.2	3.83×10^{-3}	3.10×10^{-3}	---	---	---	---
28.5	1.12×10^{-2}	8.14×10^{-3}	8.15×10^{-3}	5.75×10^{-3}	7.98×10^{-3}	4.80×10^{-3}

NOMENCLATURE

a	Radius of scatterer
C (γ)	γ -dependent parameter
CONTAM II	Computer code for predicting plume contamination from liquid monopropellant and bipropellant rocket engines on spacecraft surfaces
D	Sonic orifice diameter
D_t	Conical nozzle throat diameter
D_{eq}	Equivalent diameter defined as D for sonic orifices and $C(\gamma) D_t \cot\theta_{1/2}$ for conical nozzles
f	Rayleigh scattering function defined by Eq. (4)
g	Condensate mass fraction
I	Relative Rayleigh scattering intensity defined by Eq. (l)
I_o	Laser beam intensity
I'(), I'(\perp)	Relative Rayleigh scattering intensity, normalized to the relative Rayleigh scattering intensity of a gas sample of number density n _o , polarized parallel and perpendicular to the plane of polarization of the incident laser beam, respectively
K	Constant in Eq. (l)
k	Boltzmann's constant
MOCS	Method of characteristics solution
m₀,m₁,m₂, m₃,m₄	Scaling constants
n, n_i	Number density of gas species and i-mer number density, respectively
n(N₂)	N ₂ number density
n_o	Reservoir number density
n_t	Local total number density
P_o	Reservoir pressure

P_s	Saturation pressure
$P_{v\theta}$	Equilibrium vapor pressure at condensation onset
P_θ, P_θ^*	Pressure at condensation onset and P_θ normalized by the intermolecular potential parameter ϵ/σ^3
QCM	Quartz crystal microbalance
RVC	Research Vacuum Chamber
r	Radial distance from flow-field centerline
$(s)^\circ$	Isentropic supersaturation
$(s_\theta)^\circ$	Isentropic degrees of supercooling
T	Static temperature
T_o	Reservoir temperature
T_s	Saturation temperature
T_θ, T_θ^*	Temperature at condensation onset and T_θ normalized by the intermolecular potential parameter ϵ/k
$x; \hat{x}$	Axial position in the flow field; normalized axial position in the flow field ($\hat{x} = x/D$ for sonic orifices and $\hat{x} = x/D_t$ for conical nozzles)
\hat{x}_s	Axial location of saturation
\hat{x}_θ	Axial location of condensation onset
α, α_i	Electronic polarizability and i-mer electronic polarizability, respectively
γ	Specific heat ratio
ϵ	Well depth of Lennard-Jones intermolecular potential function
$\theta_{1/2}$	Expansion half-angle of conical nozzle
λ_o	Wavelength of incident laser beam
ρ	Depolarization ratio of Rayleigh scattering
σ	Range parameter of Lennard-Jones intermolecular potential function